JOURNAL OF AIRCRAFT
Vol. 43, No. 4, July–August 2006

# Static/Dynamic Correction Approach for Reduced-Order Modeling of Unsteady Aerodynamics

Jeffrey P. Thomas,* Earl H. Dowell,† and Kenneth C. Hall‡
*Duke University, Durham, North Carolina 27708-0300*

**Presented is a newly devised static/dynamic correction approach for eigenvector expansion based reduced-order modeling (ROM). When compared to the fundamental Ritz ROM formulation, along with the static and multiple static correction ROM approaches, the technique is demonstrated to have much better performance in modeling unsteady linearized frequency-domain aerodynamics in regions of the complex frequency plane near the imaginary axis, and up to a prescribed frequency of interest. As with the static and multiple static correction approaches, the method requires a directly computed solution at zero frequency. The method then requires one additional direct solution to be computed at some nonzero frequency, which typically is the maximum frequency of interest. When compared to the multiple static corrections method, the method circumvents the necessity of having to determine each of the multiple static corrections, which require a solution to an alternate set of equations that must be formulated and which can be costly to solve for large systems. We also consider the feasibility of using a proper orthogonal decomposition (POD) to determine approximations for the least damped fluid-dynamic eigenvectors. We demonstrate that in certain situations these approximate eigenvectors can be used in conjunction with the static/dynamic correction ROM approach to achieve an improvement in performance over the recently devised POD/ROM method where the POD shapes alone are used as ROM shape vectors. Finally, we illustrate how the method can be coupled with a structural model to compute the Mach-number flutter speed trend for a large computational-fluid-dynamics model of a three-dimensional transonic wing configuration.**

## Nomenclature

| | | |
|---|---|---|
| $\boldsymbol{A}$ | = | matrix defining homogeneous part of discretized fluid-dynamic operator |
| $\boldsymbol{\mathcal{A}}$ | = | reduced-order form of $\boldsymbol{A}$ |
| $A_R$ | = | aspect ratio, wing span squared/wing area |
| $b, c$ | = | semichord and chord, respectively |
| $\boldsymbol{b}$ | = | vector defining inhomogeneous part of discretized fluid-dynamic operator |
| $\boldsymbol{C}_Q$ | = | vector of nondimensional generalized forces |
| $\boldsymbol{I}$ | = | identity matrix |
| $J$ | = | number of cells or nodes in computational grid |
| $j$ | = | $\sqrt{-1}$ |
| $M_\infty$ | = | Mach number |
| $M$ | = | number of structural modes |
| $\boldsymbol{\mathcal{M}}$ | = | generalized mass matrix |
| $\bar{m}$ | = | mass of wing |
| $N$ | = | number of degrees of freedom for CFD model |
| $\boldsymbol{N}$ | = | vector operator defined by small-disturbance CFD model |
| $N_C$ | = | number of static corrections |
| $N_P$ | = | number of POD vectors |
| $N_R$ | = | number of eigenvectors |
| $N_S$ | = | total number of solution snapshot vectors |
| $\boldsymbol{Q}, \boldsymbol{q}$ | = | vectors for steady and small-disturbance flow solutions |
| $\boldsymbol{\mathcal{Q}}$ | = | vector of generalized forces |
| $q_\infty$ | = | freestream dynamic pressure |
| $\boldsymbol{R}$ | = | nonlinear vector operator defined by steady CFD model |
| $r$ | = | magnitude of reduced Laplace variables $\bar{s}$ |
| $\bar{s}$ | = | complex reduced frequency Laplace variable, $\bar{s} = j\bar{\omega}$ |
| $\boldsymbol{U}, \boldsymbol{u}$ | = | steady and small-disturbance conservation variables |
| $U_\infty$ | = | freestream velocity |
| $V$ | = | reduced velocity, $= U_\infty/\sqrt{(\mu)\omega_\alpha b}$ |
| $\bar{v}$ | = | volume of a truncated cone having streamwise root chord as lower base diameter, streamwise tip chord as upper base diameter, and wing half-span as height |
| $\alpha_0$ | = | airfoil or wing root steady flow angle of attack |
| $\theta$ | = | angle made by reduced Laplace variable $\bar{s}$ in complex frequency plane, $\bar{s} = re^{j\theta}$ |
| $\lambda$ | = | fluid-dynamic eigenvalue |
| $\lambda_t$ | = | wing taper ratio, $= c_t/c_r$ |
| $\mu$ | = | mass ratio $\bar{m}/\rho_\infty \bar{v}$ |
| $\xi, \boldsymbol{\xi}$ | = | structural coordinate and vector of structural coordinates |
| $\rho_\infty$ | = | freestream density |
| $\phi, \boldsymbol{\Phi}$ | = | POD vector and matrix of POD vectors |
| $\chi$ | = | POD eigenvalue |
| $\boldsymbol{\Omega}$ | = | matrix with structural frequency ratios squared along main diagonal [i.e., $(\omega_1/\omega_\alpha)^2, \ldots, (\omega_M/\omega_\alpha)^2$] |
| $\omega, \bar{\omega}$ | = | frequency and reduced frequency, $\bar{\omega} = \omega c/U_\infty$ (airfoil) $\bar{\omega} = \omega b/U_\infty$ (wing) |
| $\omega_\alpha$ | = | wing first torsional mode natural frequency |

*Subscripts and Superscripts*

| | | |
|---|---|---|
| $H$ | = | Hermitian transpose |
| $r, t$ | = | root and tip, respectively |
| $s, d$ | = | static and dynamic, respectively |

## Introduction

CONTINUAL efforts to better understand and predict the aeroelastic behavior of aerospace vehicles have made unsteady aerodynamic modeling an area of active research over the last several decades. And although numerical techniques and computer power are moving towards a level where time-dependent fully coupled structural and fluid-dynamic simulations of realistic configurations are becoming feasible, such calculations are still far from being practical.

Frequency-domain methods have been more widely used, and rational polynomial curve-fit methods for modeling the unsteady

Received 1 May 2001; accepted for publication 24 June 2004. 

*Research Assistant Professor, Department of Mechanical Engineering and Materials Science. Member AIAA.

†J. A. Jones Professor, Department of Mechanical Engineering and Materials Science, and Dean Emeritus, School of Engineering. Fellow AIAA.

‡Professor, Department of Mechanical Engineering and Materials Science. Associate Fellow AIAA.

aerodynamics have proven useful. For these methods, tabulated aerodynamic data computed for real frequencies are used to model the unsteady aerodynamics for complex frequencies. These methods include Roger's[1] common denominator least-squares technique, various matrix Padé approximant methods as proposed by Vepa,[2] Edwards,[3] and Karpel,[4] and finally the minimum-state technique developed by Karpel.[4] For each of these techniques, best approximations are determined in a least-squares sense to tabulated unsteady aerodynamic force data.

In recent years, eigenvector-based reduced-order modeling approaches also have proven to be a valuable tool for greatly reducing the computational expense of modeling unsteady frequency-domain fluid dynamics. Extensive research efforts by Dowell, Hall, Florea, Romanowski, and others[5–11] have demonstrated that models of unsteady fluids problems with on the order of tens of thousands of degrees of freedom (DOF) can be reduced to systems with on the order of just a few dozen DOF while still maintaining high solution accuracy.

In this paper, we illustrate how a newly devised blended static and dynamic correction approach can substantially improve the performance of an eigenvector-based reduced-order modeling (ROM). We further illustrate how proper-orthogonal-decomposition vectors can be used to determine approximations of the full system eigenvectors, which in turn can be used with the static/dynamic correction ROM to improve performance in some cases over the recently devised proper-orthogonal-decomposition (POD)/ROM method (see Refs. 12–14). We also demonstrate how the method can be coupled with a structural dynamic model, a transonic wing configuration in this instance, for aeroelastic stability analysis. The reduced-order-model methods all show substantial reductions in computational costs over conventional methods of flutter analysis using computational-fluid-dynamics (CFD)-based aerodynamic models. The present paper explores how these reduced-order models can be further improved to reduce computational costs.

## Governing Equations

In the following, we consider inviscid unsteady small disturbance flows linearized about a nonlinear steady background flow. Considering also harmonic motion, one can arrive at a set of frequency-domain equations governing the unsteady small-disturbance flow for some prescribed reduced frequency $\bar{\omega}$. For most conventional CFD methods, the dependent flow variables are solved at discrete locations on a computational mesh encompassing the physical domain of interest. The steady and unsteady flow solver variables can be thought of as $N$-dimensional vectors of the form

$$\boldsymbol{Q} = \begin{Bmatrix} \boldsymbol{U}_1 \\ \boldsymbol{U}_2 \\ \vdots \\ \boldsymbol{U}_J \end{Bmatrix} \qquad \text{and} \qquad \boldsymbol{q} = \begin{Bmatrix} \boldsymbol{u}_1 \\ \boldsymbol{u}_2 \\ \vdots \\ \boldsymbol{u}_J \end{Bmatrix} \tag{1}$$

where $\boldsymbol{U}_j$ and $\boldsymbol{u}_j$ are the vectors of steady and unsteady dependent conservation variables stored at each mesh node or cell location $j$, and $N$ is the number of dependent flow variables times the number mesh points. The steady $\boldsymbol{R}$ and unsteady $\boldsymbol{N}$ CFD flow solvers represent nonlinear and linear residual operators of the form

$$\boldsymbol{R}(\boldsymbol{Q}) = \boldsymbol{0} \qquad \text{and} \qquad \boldsymbol{N}(\boldsymbol{q}; \boldsymbol{Q}, \bar{\omega}, \Delta) = \boldsymbol{0} \tag{2}$$

where for the unsteady solver $\Delta$ represents the particular unsteady motion under consideration (e.g., pitching motion, plunging motion, etc.). The linear unsteady solver residual operator can be further expanded as

$$\boldsymbol{N}(\boldsymbol{q}; \boldsymbol{Q}, \bar{\omega}, \Delta) = \boldsymbol{A}(\boldsymbol{Q}, \bar{\omega})\boldsymbol{q} - \boldsymbol{b}(\boldsymbol{Q}, \bar{\omega}, \Delta) = \boldsymbol{0} \tag{3}$$

where $\boldsymbol{A}(\boldsymbol{Q}, \bar{\omega})$ is the $N \times N$ unsteady fluid dynamic influence matrix, which is the Jacobian of the unsteady solver residual operator with respect to the unsteady flow variables, that is,

$$\boldsymbol{A}(\boldsymbol{Q}, \bar{\omega}) = \frac{\partial \boldsymbol{N}(\boldsymbol{q}; \boldsymbol{Q}, \bar{\omega}, \Delta)}{\partial \boldsymbol{q}}$$

and $\boldsymbol{b}(\boldsymbol{Q}, \bar{\omega}, \Delta)$ is a $N \times 1$ vector, which like the matrix $\boldsymbol{A}$ is also dependent on the background steady flow $\boldsymbol{Q}$ and unsteady frequency $\bar{\omega}$, in addition to the unsteady motion under consideration $\Delta$. Note, one does not typically form $\boldsymbol{A}$ or $\boldsymbol{b}$ because of the large number of degrees of freedom normally considered in a realistic CFD model.

If we next consider a linearized unsteady frequency-domain CFD flow solver, which happens to be first order in frequency $\bar{\omega}$, then one can expand the fluid-dynamic influence matrix $\boldsymbol{A}(\boldsymbol{Q}, \bar{\omega})$ as

$$\boldsymbol{A}(\boldsymbol{Q}, \bar{\omega}) = \boldsymbol{A}_1(\boldsymbol{Q}) - j\omega \boldsymbol{A}_1(\boldsymbol{Q})$$

Also, for a first order in frequency method, the vector $\boldsymbol{b}$ can be expanded as

$$\boldsymbol{b}(\boldsymbol{Q}, \bar{\omega}, \Delta) = \boldsymbol{b}_1(\boldsymbol{Q}, \Delta) - j\omega \boldsymbol{b}_1(\boldsymbol{Q}, \Delta)$$

If $\bar{s}$ represents the complex reduced frequency $j\bar{\omega}$, then the resulting linear algebraic system representation for a first order in frequency unsteady solver can be written as

$$(\boldsymbol{A}_0 - \bar{s}\boldsymbol{A}_1)\boldsymbol{q} = \boldsymbol{b}_0 + \bar{s}\boldsymbol{b}_1 \tag{4}$$

Further details on the development of the linearized frequency-domain unsteady fluid-dynamic equations and their discrete CFD counterpart can be found in Hall et al.[13] and Thomas et al.[14]

Note, depending on the particular CFD algorithm used, a given linearized unsteady frequency-domain CFD method can be a more general function of frequency $\bar{\omega}$. This for instance is the case for the unsteady CFD method used for the transonic wing configuration presented later in this paper. For this particular unsteady solver, the CFD method (Lax–Wendroff) is actually second order in frequency. However, a state-space model can be easily devised, and the same basic ROM methodologies that are presented in the next section can be similarly applied. More details are presented in the section of this paper concerning the transonic wing.

## Eigenvector-Based Reduced-Order-Modeling Strategies

A number of eigenvector-based ROM strategies are available for solving Eq. (4). Here we outline a few of these approaches in addition to introducing the static/dynamic correction method.

### Basic Eigenvector ROM Approach

In what we will denote as the "basic" ROM approach, the reduced-order-model method takes the form of a standard Ritz expansion where the unsteady flow variables $\boldsymbol{q}$ are expressed as an eigenmode series expansion of the form

$$\boldsymbol{q} = \sum_{n=1}^{N} \boldsymbol{r}_n v_n \tag{5}$$

Here, $v_n$ are the weights of each corresponding right eigenvector $\boldsymbol{r}_n$ in the expansion. The right eigenvectors come from the generalized eigenvalue problem defined by the homogeneous case of Eq. (4), that is,

$$(\boldsymbol{A}_0 - \lambda_n \boldsymbol{A}_1)\boldsymbol{r}_n = \boldsymbol{0} \tag{6}$$

where $\lambda_n$ is the eigenvalue corresponding the right eigenvector $\boldsymbol{r}_n$. A similar equation holds for the $1 \times N$ left eigenvectors $\boldsymbol{l}_n$, that is,

$$\boldsymbol{l}_n(\boldsymbol{A}_0 - \lambda_n \boldsymbol{A}_1) = \boldsymbol{0}^H \tag{7}$$

The modal weights $v_n$ can be determined by substituting Eq. (5) into Eq. (4) and premultiplying the resulting equation by the corresponding left eigenvectors suitably normalized such that $\boldsymbol{l}_n \boldsymbol{A}_1 \boldsymbol{r}_n = 1$. This yields the basic Ritz form ROM modal weights as

$$v_n = [1/(\lambda_n - \bar{s})]\boldsymbol{l}_n \cdot (\boldsymbol{b}_0 + \bar{s}\boldsymbol{b}_1) \tag{8}$$

We will show subsequently that the convergence of the basic Ritz formulation ROM, at least in the case of the airfoil flow compressible fluid-dynamic models we have investigated, turns out to be rather

poor. In fact, we have found that in most cases, many if not all of the system eigenmodes must be used in the ROM to obtain a favorable level of accuracy.

As a note, in judging the performance of a ROM, one not only has to consider how many eigenvectors are required to achieve a prescribed level of accuracy, but one must also consider in what region of the complex frequency plane it is desired to maintain this level of accuracy. For aeroelastic stability analysis, the unsteady solution $\boldsymbol{q}$ is typically required only near the imaginary axis in the complex reduced frequency plane. Furthermore, there will typically be some upper limit in reduced frequency where, because of the coarseness of the computational mesh, the unsteady CFD model of the fluid dynamics begins to significantly lose accuracy.

One way to improve the performance of the basic Ritz ROM formulation is to force the expansion to be exact at some location in the complex frequency plane. The origin is a good place for instance, and this in fact leads to the static correction ROM approach.

#### Static Correction Approach

In an effort to improve the performance of the eigenvector ROM near the imaginary axis, one can instead express the eigenmode expansion as

$$\boldsymbol{q} = \boldsymbol{q}_s + \sum_{n=1}^{N} v_n \boldsymbol{r}_n \tag{9}$$

where $\boldsymbol{q}_s$ is known as the static solution, which is the solution for $\bar{s} = 0$ computed directly from the unsteady CFD flow solver. In this form, Eq. (9) ensures that the ROM is always exact for the case of zero frequency no matter how many eigenmodes are used in the expansion. Substituting Eq. (9) into Eq. (4), and again using the orthogonal properties of the left and right eigenvectors, yields the expansion weights for the static correction ROM as

$$v_n = [\bar{s}/(\lambda_n - \bar{s})]\boldsymbol{l}_n \cdot [(1/\lambda_n)\boldsymbol{b}_0 + \boldsymbol{b}_1] \tag{10}$$

#### Multiple Static Corrections Approach

Although, and as will be shown, the performance of the static correction method is a significant improvement over the basic ROM strategy, further improvement, especially for modeling at higher frequencies, can be realized by using a technique known as the method of multiple static corrections.[9] The technique stems from the ability to rewrite the terms $1/(\lambda_n - \bar{s})$, which appear in both the basic and static correction ROM expansions as

$$1/(\lambda_n - \bar{s}) = (\bar{s}/\lambda_n)[1/(\lambda_n - \bar{s})] + (1/\lambda_n) \tag{11}$$

Substituting Eq. (11) into Eq. (10), and subsequently Eq. (9), yields the expansion for $\boldsymbol{q}$ as

$$\boldsymbol{q} = \boldsymbol{q}_s + \sum_{n=1}^{N} \left(\frac{\bar{s}}{\lambda_n}\right)^2 \frac{\boldsymbol{l}_n \cdot (\boldsymbol{b}_0 + \lambda_n \boldsymbol{b}_1)}{\lambda_n - \bar{s}} \boldsymbol{r}_n + \bar{s} \sum_{n=1}^{N} \frac{1}{\lambda_n^2} (\boldsymbol{l}_n \cdot \boldsymbol{b}_0)\boldsymbol{r}_n + \bar{s} \sum_{n=1}^{N} \frac{1}{\lambda_n} (\boldsymbol{l}_n \cdot \boldsymbol{b}_1)\boldsymbol{r}_n \tag{12}$$

One can then define

$$\boldsymbol{q}_s^{(2)} = \sum_{n=1}^{N} \frac{1}{\lambda_n^2} (\boldsymbol{l}_n \cdot \boldsymbol{b}_0)\boldsymbol{r}_n \tag{13}$$

where $\boldsymbol{q}_s^{(2)}$ is referred to as the "second" static correction. It can be shown that $\boldsymbol{q}_s^{(2)}$ is the solution of the linear system

$$\boldsymbol{A}_0 \boldsymbol{q}_s^{(2)} = \boldsymbol{A}_1 \boldsymbol{q}_s^{(1)} \tag{14}$$

In this instance, $\boldsymbol{q}_s^{(1)}$ is the "first" static solution, which corresponds to the nominal static solution $\boldsymbol{q}_s$.

When the multiple static corrections approach is applied $N_C$ times, the expansion for $\boldsymbol{q}$ can be expressed as

$$\boldsymbol{q} = \sum_{l=1}^{N_C} \bar{s}^{(l-1)} \boldsymbol{q}_s^{(l)} + \sum_{n=1}^{N} \left(\frac{\bar{s}}{\lambda_n}\right)^{N_C} \frac{\boldsymbol{l}_n \cdot (\boldsymbol{b}_0 + \lambda_n \boldsymbol{b}_1)}{\lambda_n - \bar{s}} \boldsymbol{r}_n + \sum_{l=1}^{N_C} \sum_{n=1}^{N} \left(\frac{\bar{s}}{\lambda_n}\right)^{l} (\boldsymbol{l}_n \cdot \boldsymbol{b}_1)\boldsymbol{r}_n \tag{15}$$

where each subsequent static correction is given by the recursive relation

$$\boldsymbol{A}_0 \boldsymbol{q}_s^{(l)} = \boldsymbol{A}_1 \boldsymbol{q}_s^{(l-1)} \tag{16}$$

As will be shown subsequently, the technique of multiple static corrections does indeed help to improve ROM performance especially for higher frequencies; however, the necessity of having to formulate and then solve the system in Eq. (16) unfortunately tends to make the method an expensive option for large systems.

#### Combined Static and Dynamic Correction ROM Approach

As a new approach, we have discovered a convenient way to improve ROM performance is to simply fix the ROM to be exact at the end points of a given frequency interval of interest. Much like the static correction method forces the ROM to always be exact for $\bar{s} = 0$, the idea now however is to combine a static $\boldsymbol{q}_s$ and a dynamic $\boldsymbol{q}_d$ solution into the ROM expansion, that is,

$$\boldsymbol{q} = \left(1 - \frac{\bar{s}}{\bar{s}_d}\right)\boldsymbol{q}_s + \frac{\bar{s}}{\bar{s}_d}\boldsymbol{q}_d + \sum_{n=1}^{N} v_n \boldsymbol{r}_n \tag{17}$$

where $q_d$ is the solution computed directly from the unsteady CFD flow solver for a frequency of $s = s_d$. In this form, the static and dynamic solutions are incorporated into the ROM (i.e., turned "on" and "off") at their respective frequencies. Substituting Eq. (17) into the governing linearized unsteady frequency-domain fluid-dynamic equation [Eq. (4)] and again using the orthogonal properties of the left and right eigenvectors, yields the expansion weights of static/dynamic correction ROM approach as

$$v_n = \left(\frac{\bar{s}^2}{\bar{s}_d} - \bar{s}\right)\left(\frac{1}{\lambda_n - \bar{s}}\right)\left[\frac{\boldsymbol{l}_n \cdot (\boldsymbol{b}_0 + \bar{s}_d \boldsymbol{b}_1)}{\lambda_n - \bar{s}_d} - \frac{\boldsymbol{l}_n \cdot \boldsymbol{b}_0}{\lambda_n}\right] \tag{18}$$

It will be shown in the following section that this extremely simple modification has the effect of significantly improving the accuracy of the ROM. All of this is achieved for only the cost of one extra dynamic ($\bar{\omega} \neq 0$) solution via the unsteady CFD flow solver and without the extra computational effort necessary to determine multiple static corrections.

We have also considered the possibility of using multiple dynamic corrections and have found that further improvement in overall ROM performance is feasible. For the purpose of this paper however, we choose to focus solely on the static and single dynamic correction form for illustrative purposes in comparing the basic methodology to the other ROM techniques and in demonstrating how the methodology can be coupled with a frequency-domain structural model for the ultimate purpose of aeroelastic modeling.

## Isolated Airfoil Model Problem

As a first test case to demonstrate the capabilities of the various ROM strategies, we consider a somewhat coarse-mesh CFD model for the inviscid flow about a NACA 64A010 airfoil at a zero-degree angle of attack for various steady background flow Mach numbers. In this instance, the CFD method is an explicit, cell-centered, finite volume Godunov[15] based method utilizing Roe's[16] approximate Riemann solver in conjunction with van Leer's[17] technique for preserving monotonicity and better than first-order accuracy. At transonic Mach numbers, shocks are present, and the steady flow per se is highly nonlinear.

Shown in Fig. 1 are close-up and overall illustrations of the computational mesh used. The O-type mesh consists of 32 cells circumferentially and 16 cells radially for a total of 512 cells. With four

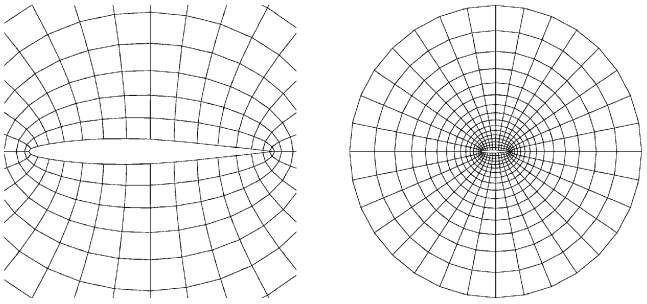

**a) Close-up** **b) Overall**

**Fig. 1 Mesh layout for NACA 64A010 airfoil grid test case: 32 × 16 computational cells.**

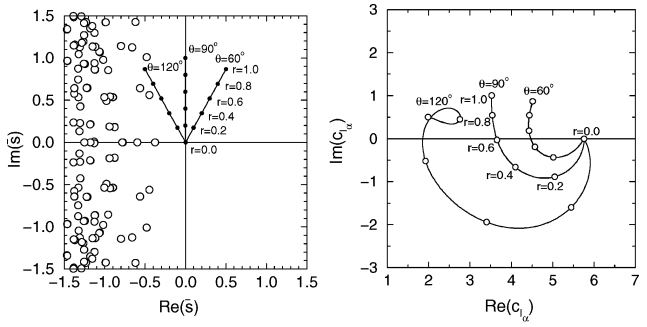


**a) $M_\infty = 0.3$ eigenspectrum** **c) $M_\infty = 0.9$ eigenspectrum**

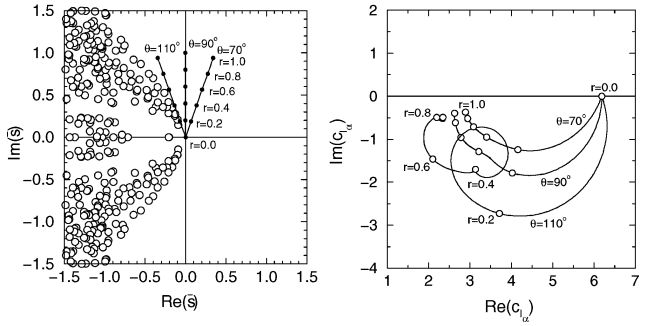


**b) $M_\infty = 0.3$ transfer function** **d) $M_\infty = 0.9$ transfer function**

**Fig. 2 Full system eigenspectrums and lift caused by pitch transfer functions: NACA 64A010 airfoil section, $\alpha_0 = 0$ (deg), 32 × 16 computational cells.**

dependent variables (density, $x$ and $y$ momentum components, and total energy) stored at each cell location, the total number of dependent variables (DOF) is 2048. Even though the mesh is rather coarse, the size of the system provides a sufficiently accurate model of the steady and unsteady flows for illustrative purposes while being small enough in size so that computation of all of the system eigenmodes and eigenvalues via a standardized eigensolver software library (LAPACK[18]) is still feasible.

Figure 2 shows the fluid-dynamic eigenspectrums (Figs. 2a and 2c) and full system unsteady lift caused by unit pitch transfer function (Figs. 2b and 2d) for $M_\infty = 0.3$ and 0.9. The transfer function curves represent the real and imaginary parts of lift caused by unit pitch for complex reduced frequencies along specific paths in the complex $\bar{s}$ plane. For $M_\infty = 0.3$, results are shown along the paths $\bar{s} = re^{j\theta}$ for the angles $\theta = 90$, 60, and 120 deg as $r$ ranges from zero to one. For $M_\infty = 0.9$, note that the $\theta = 120$ deg path traverses through the large concentration of eigenvalues that occur near the origin for this Mach number. The behavior of the transfer function becomes very complex along this path. We instead consider the paths $\theta = 90$, 70, and 110 deg again as $r$ ranges from zero to one (Fig. 2c).

In investigating several different Mach numbers (not shown here), we have found there is a tendency for the eigenvalues to congregate towards the origin of the complex frequency plane with increasing Mach number. This is evident in Fig. 2. As will be shown subsequently, this leads to the general tendency of there being a greater number of eigenmodes needed in the various ROM methods at higher transonic Mach numbers.

### Performance Trends for the Various Reduced-Order-Modeling Strategies

Figure 3 demonstrates the accuracy trends for the various ROM strategies as applied to the NACA 64A010 airfoil configuration for a Mach number of $M_\infty = 0.3$. The first row of subfigures shows the full system fluid-dynamic eigenspectrums (open circles) along with the eigenvalues (closed circles) corresponding to the particular eigenmodes that have been used for the various ROM techniques. Rows two through five show ROM results for the basic, one static correction, three static corrections ($N_C = 3$), and the static/dynamic correction (with $\bar{s}_d = j$) ROM approaches, respectively. In Fig. 3, columns one, two, and three correspond to results when using one, two, and three eigenmodes for each of the ROM methods. The particular eigenmodes again correspond to the eigenvalues indicated in the first row of eigenspectrum plots.

As can be seen, the basic ROM approach performance is very poor for this particular problem. In fact, we have found that nearly all 2048 eigenvectors must be used to obtain an accurate solution. Note however that the general trends of the ROM transfer function curves all tend to be very similar to the exact solution's shapes. Furthermore, the trends of the ROM transfer function curves do not change all that much depending on the number of eigenvectors used.

This has led us to believe that most of the dominant unsteady dynamics that affects the region of the complex frequency plane near the imaginary axis is associated with the eigenmode corresponding to the least damped eigenvalue with zero imaginary frequency component, particularly in subsonic cases where the eigenspectrum tends to be much more spread out than for higher Mach-number flows, and where typically there is one eigenvalue with zero imaginary frequency component that is also usually the least damped eigenvalue for the whole system.

From the third row of figures, it can be seen that the static correction ROM, because of its construction, matches the exact solution at a zero frequency. This helps to significantly improve accuracy for low frequencies when compared to the basic ROM approach. However, for higher frequencies the performance of the static correction ROM is still rather poor. As we have found with the basic ROM approach, almost all of the eigenvectors must be used to approach the exact solution. Note once again, the basic trends of the ROM transfer function curves do not change all that much with varying numbers of eigenmodes used in the expansion.

The multiple static corrections (three in this case) ROM is a further improvement; however, the method still has difficulties for the higher frequencies. Furthermore, the method can be prohibitively expensive for large systems because of the necessity of having to formulate and solve Eq. (16) for each additional static correction.

From the last row of figures, it can be seen how the static/dynamic ROM approach has the best performance of any of the ROM strategies. In this instance, the dynamic frequency has been chosen to be $\bar{s}_d = j$ (i.e., $\bar{\omega}_d = 1$). For the cost of computing only one additional nonzero frequency solution, the difficulty of having to solve for multiple static corrections is circumvented, and in this instance a greater level of overall accuracy is obtained when compared to any of the other ROM approaches.

Figure 4 shows a comparison of the static/dynamic method ROM results for the lift caused by pitch transfer function when using zero and one eigenvector. As can be seen for the zero eigenvector case (Fig. 4a), the ROM result is simply a linear interpolation between the zero and dynamic frequency ($\bar{s} = j$) lift caused by pitch solutions. Interestingly, just the single eigenvector associated with the least damped eigenmode is able to improve the ROM to the level accuracy shown in Fig. 4b (also Fig. 3e). For this subsonic case, most of the dominant unsteady dynamics can be seen to reside in the least damped eigenmode of the system.

Next, Fig. 5 shows the same pattern of results as Fig. 3 except now for the case of a $M_\infty = 0.9$ background flow. The important thing to note here is the need for a greater number of eigenmodes to be

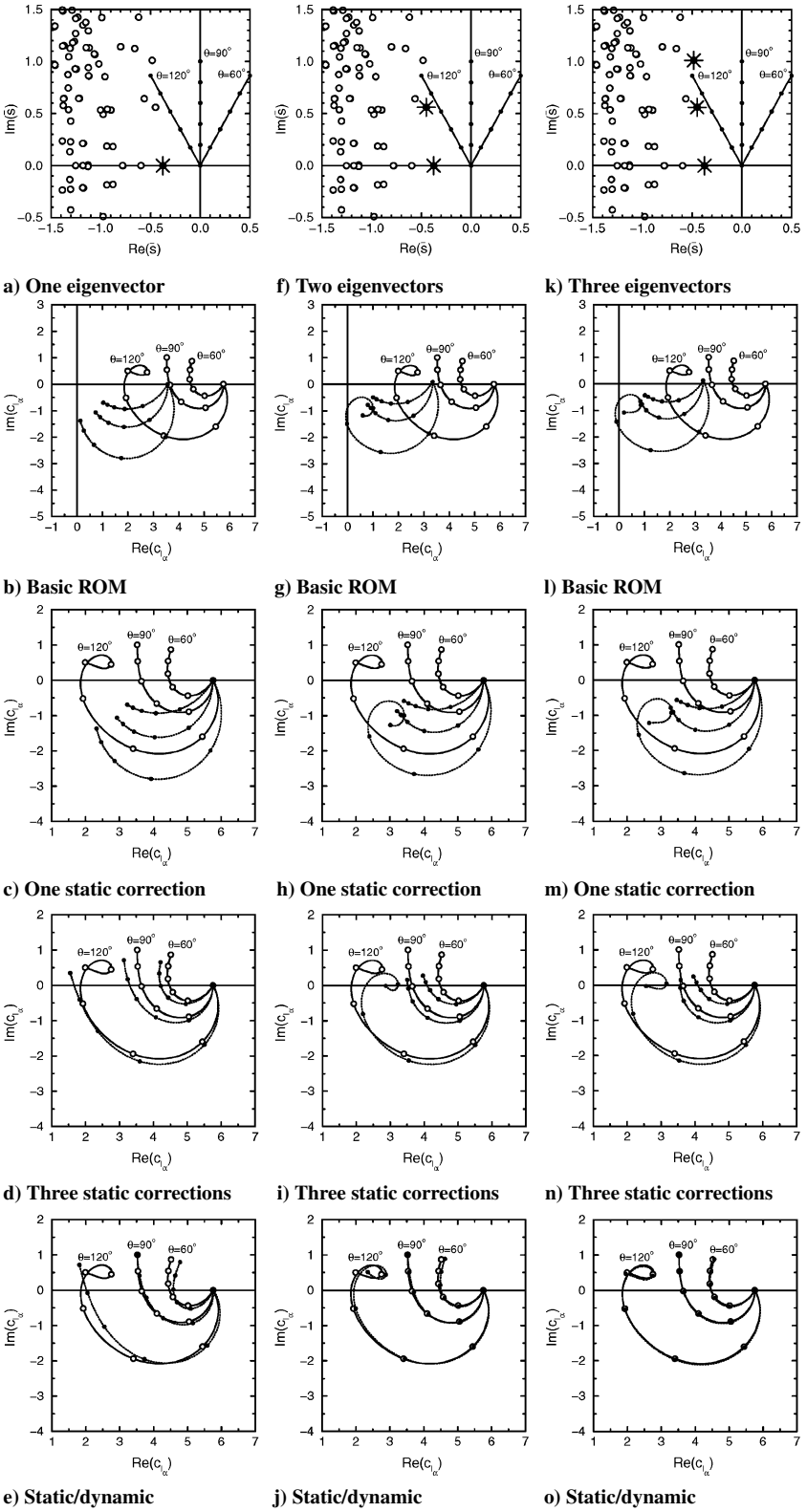


**Fig. 3 Various ROM strategies accuracy characteristics: NACA 64A010 airfoil section, $M_\infty = 0.3$, $\alpha_0 = 0$ (deg), 32 × 16 computational cells.**

used in each of the ROM strategies for this higher transonic Mach number. This is because of the greater concentration of eigenvalues near the origin. Yet once again, it can be seen that the static/dynamic ROM has the best performance.

Furthermore, especially in cases such as this $M_\infty = 0.9$ example where a large number of eigenmodes are required, we have found it is important to also consider the manner in which the eigenmodes are sequenced in the ROM expansion. For the results shown in Fig. 5, we have ordered the eigenmodes in each of the ROM techniques with respect to the ever-increasing distance of their corresponding eigenvalues from the location $\bar{s} = j/2$, (i.e., $\frac{1}{2}$ of the maximum frequency of interest in this case) in the complex frequency plane.

We found that in many cases where there tend to be dense eigenspectrums, a somewhat better way to sequence the eigenmodes is to use the same approach, yet always have the least damped mode with zero imaginary component come first in the sequence. Once again,

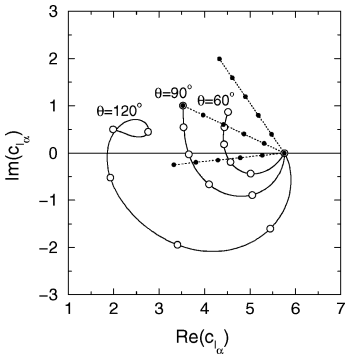


a) Zero eigenvectors

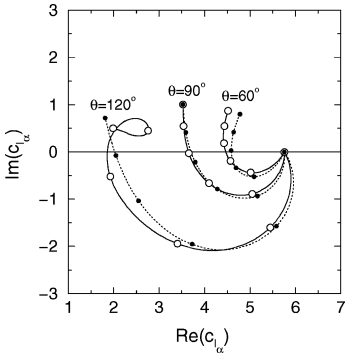


b) One eigenvector

**Fig. 4 Comparison of static/dynamic correction method ROM lift caused by pitch transfer function when using zero and one eigenvector: NACA 64A010 airfoil section, $M_\infty = 0.3$, $\alpha_0 = 0$ (deg), 32 × 16 computational cells.**

even in these transonic cases where there can be eigenvalues with less damping, and with nonzero frequency (i.e. nonzero imaginary component), the least damped mode with zero frequency still tends to dominate much of the unsteady dynamics.

It is often interesting to consider the ROM accuracy trend as an ever-increasing number of eigenmodes are used in the ROM expansions. The $M_\infty = 0.3$ case provides an ideal demonstration. Figure 6 shows a comparison of accuracy trends for the $L_2$ error norm of all four possible transfer functions (i.e., $\bar{c}_{l_{h/b}}$, $\bar{c}_{l_\alpha}$, $\bar{c}_{m_{h/b}}$, and $\bar{c}_{m_\alpha}$) along the specified paths in the complex frequency plane as shown in Fig. 2. As can be seen, a large increase in accuracy is apparent after just the first few eigenmodes are used in the various ROM techniques, and again, those being the eigenmodes with eigenvalues close to the region of the complex frequency plane of interest. In this case, $\bar{s} = j/2$. After that, the improvement in accuracy levels off. The eigenmodes with eigenvalues away from the region of interest tend to affect the ROM to much lesser degree, as expected.

Figure 7 is presented to give the reader an idea as to the overall extent of the eigenvalue constellations. In the sequence of subfigures of Fig. 7, we show an ever-increasing region of the complex frequency plane. The inner box in each subfigure of Fig. 7 shows the original region of the complex plane of interest (i.e., Fig. 2a). As can be seen, for this subsonic case the majority of the eigenspectrum lies outside the region of the complex frequency plane of interest. The transonic case is much the same, although the convergence is slower because many more eigenvalues are situated in the region of interest.

## Approximate Eigenvectors Using Proper-Orthogonal-Decomposition Technique

For large systems, determining the eigeninformation directly can be difficult, costly, and if the system is too large, simply impossible. To add to the difficulty, even though the fluid-dynamic matrices $\boldsymbol{A}_0$ and $\boldsymbol{A}_1$ are sparse, they are in general nonsymmetric, and eigensolver techniques such as those used by LAPACK[18] typically require $\mathcal{O}(N^3)$ operations.

Some newly developed methods that are capable of determining a limited number of eigenmodes and eigenvectors for very large (order millions of DOF) sparse systems are becoming available and in fact can be found in public-domain software libraries such as ARPACK.[19] These techniques however only yield the right eigenvectors. To obtain the necessary left eigenvectors, one must assemble an alternate solver that represents the adjoint of the original unsteady CFD method, that is,

$$\boldsymbol{N}(\boldsymbol{q})^H = \boldsymbol{q}^H \left( \boldsymbol{A}_0^H - \bar{s} \boldsymbol{A}_1^H \right) - \boldsymbol{b}^H \tag{19}$$

This can be a difficult task as it amounts to having to create a residual solver where the entire algorithm represents the precise Hermitian transpose of the original unsteady flow solver residual operator.

Fortunately, there is an alternative to a full system eigensolution where one can still sort out the dominant (least damped) eigenmodes. The method is based on the concept of assembling an ensemble of solution snapshots (i.e., directly computed solutions via the unsteady CFD solver for various frequencies and excitations). Next, a proper orthogonal decomposition is used to derive a set of optimal shape vectors (POD vectors). These POD shapes will then carry, in ordered fashion, the most dominant unsteady dynamic modal characteristics of the unsteady flows. A recently published text by Holmes et al.[20] provides an overview of the POD method along with extensive details of how the method has been used by researchers to study a wide variety of fluids problems. Furthermore, recent articles by Kim,[12] Hall et al.,[13] and Thomas et al.[14] each provide in-depth discussions of how the POD method can be used to generate shape vectors that can be used like eigenvectors for reduced-order modeling. (This technique is generally referred to as the POD/ROM method.) Here we describe some of the more significant steps of how POD shapes are constructed.

First, an ensemble of $N_S$ unsteady flow solutions is computed at a given Mach number for a number of frequencies and excitations. The frequencies are typically taken in equal increments over a frequency range of interest, and the excitations are usually chosen to be structural motions or mode shapes of the configuration under consideration.

The POD shapes $\phi_k$ are based on an expansion of these solution snapshots, namely,

$$\phi_k = \sum_{n=1}^{N_S} \boldsymbol{q}^n w_k^n \qquad k = 1, 2, 3, \ldots, N_S \tag{20}$$

where $w_k^m$ is the contribution of the $m$th snapshot to the $k$th POD vector. This expansion can also be written as

$$\phi_k = \boldsymbol{S} \boldsymbol{w}_k \tag{21}$$

where

$$\boldsymbol{S} = \begin{bmatrix} | & | & & | \\ \boldsymbol{q}^1 & \boldsymbol{q}^2 & \cdots & \boldsymbol{q}^{N_S} \\ | & | & & | \end{bmatrix} \qquad \text{and} \qquad \boldsymbol{w}_k = \begin{Bmatrix} w_k^1 \\ w_k^2 \\ \vdots \\ w_k^M \end{Bmatrix} \tag{22}$$

The weights $w_k^m$ are determined by solving a $N_S$ degree-of-freedom eigenvalue problem

$$\boldsymbol{S}^H \boldsymbol{S} \boldsymbol{w}_k = \chi_k \boldsymbol{w}_k \tag{23}$$

Equation (23) defines an eigenvalue problem for the POD eigenvectors $\boldsymbol{w}_k$ and eigenvalues $\chi_k$ (not to be confused with the fluid-dynamic system eigenvalues $\lambda_n$ and eigenvectors $\boldsymbol{r}_k$). It can be shown that the snapshots $\boldsymbol{q}^m$ will have the tendency to lie in a subspace spanned by the POD shape vectors $\phi_k$ with the largest POD eigenvalues $\chi_k$. Equation (23) can be quickly solved because the total number of snapshots $N_S$ is typically on the order of 10 to 100.

To demonstrate the method, we again consider the coarse-mesh airfoil problem of the preceding section. Here we show how one can

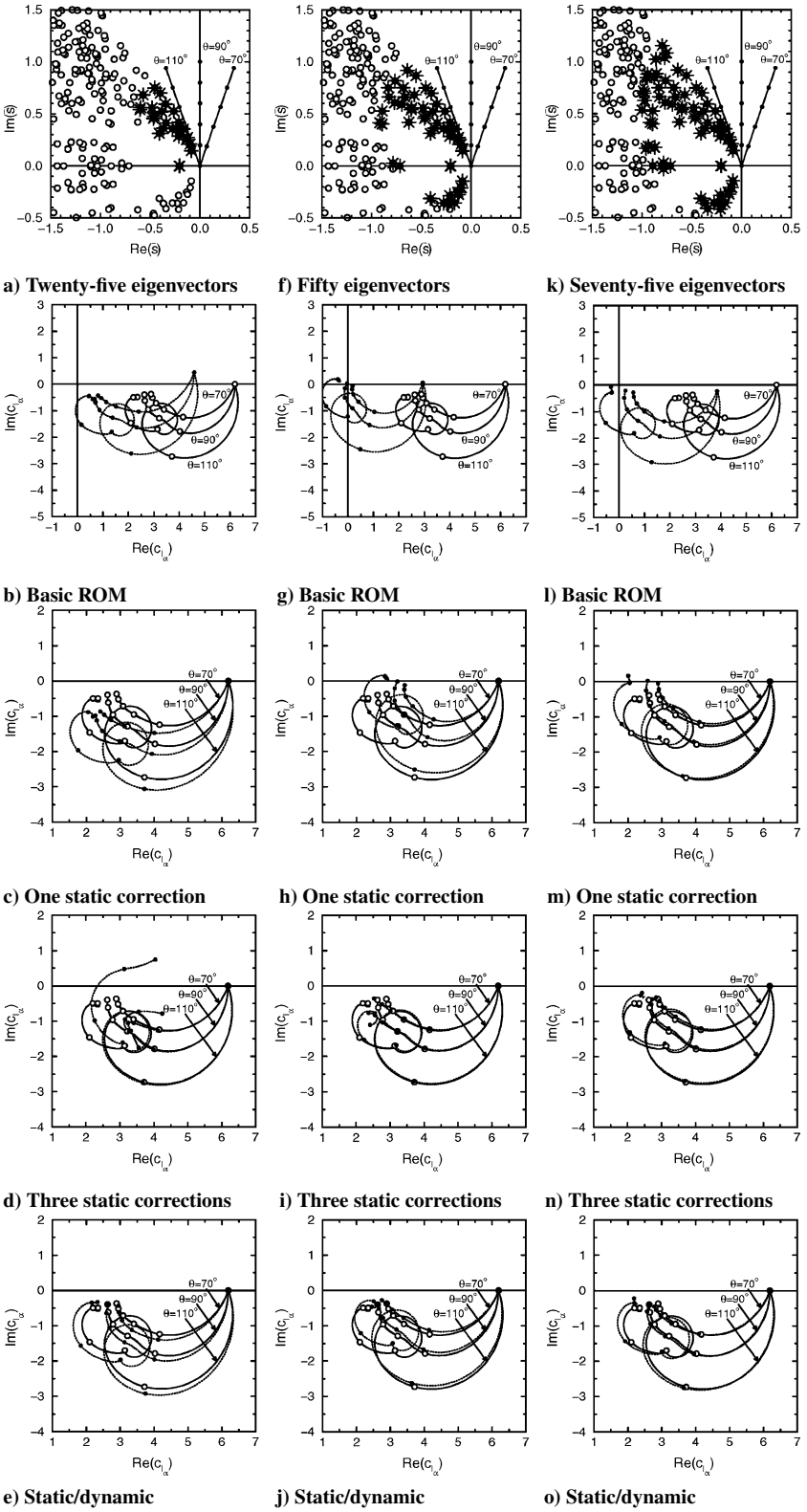


**Fig. 5 Various ROM strategies accuracy characteristics: NACA 64A010 airfoil section, $M_\infty = 0.9$, $\alpha_0 = 0$ (deg), 32 × 16 computational cells.**

recover the dominant eigenvalues and eigenvectors of the full system model by using the solution snapshots and the proper-orthogonal-decomposition method. First, we compute a number of unsteady flow solutions for plunge-and-pitch airfoil motions. We consider the reduced frequency range of interest to be between zero and one, and we compute unsteady solutions via the CFD solver for an increment of 1/16 in reduced frequency (i.e., $\Delta\bar{\omega} = 1/16 = 0.0625$) for both pitch-and-plunge motions. This corresponds to a total of 16 plunge snapshots (the zero-frequency solution is trivial) and 17 pitch snapshots. The solutions for the corresponding negative frequencies are the complex conjugates of their positive frequency counterparts. Thus an additional 16 plunge-and-pitch snapshots can be added to the overall ensemble for a total for 63 snapshots. We can also consider larger frequency increments such as $\Delta\bar{\omega} = 0.125$, $\Delta\bar{\omega} = 0.25$, $\Delta\bar{\omega} = 0.5$, which result in ensembles of 33, 17, and 9 total snapshots, respectively.

In addition to identifying the dominant unsteady fluid dynamics, the POD has the ability to indicate whether the snapshot ensemble

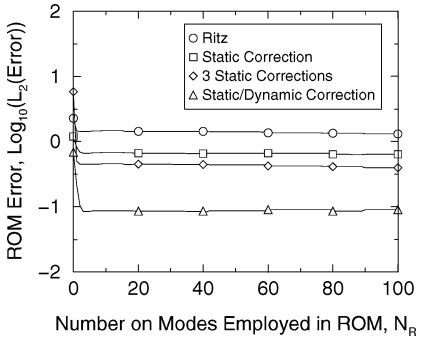


**Fig. 6 Comparison of accuracy trends for the various ROM methods when using an ever-increasing number of eigenmodes: NACA 64A010 airfoil section, $M_\infty = 0.3$, $\alpha_0 = 0$ (deg), 32 × 16 computational cells.**

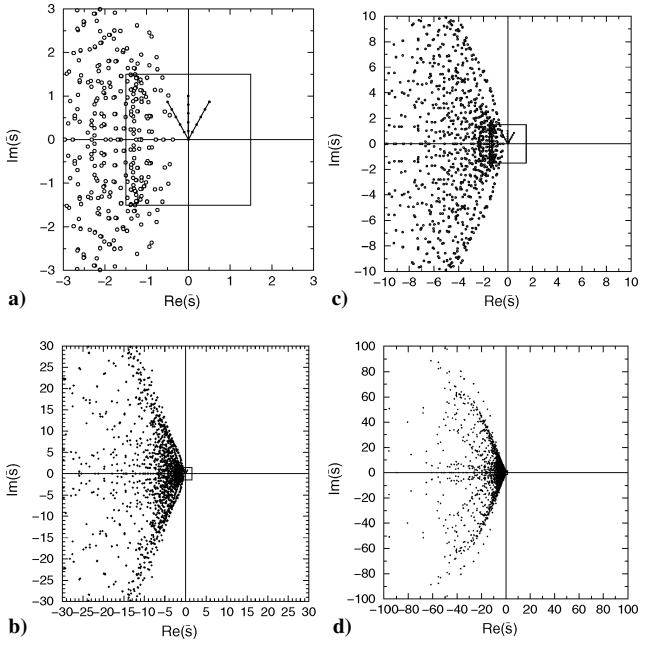


**Fig. 7 Full system eigenspectrum $M_\infty = 0.3$: NACA 64A010 airfoil section, $\alpha_0 = 0$ (deg), 32 × 16 computational cells.**

is of sufficient frequency resolution. It can also indicate if too many snapshots are being considered. This comes from an examination of the POD eigenvalues $\chi_k$. Figure 8 shows the magnitude of the POD eigenvalues for each frequency increment snapshot ensemble. The POD eigenvalues are all real and positive, and in this instance the POD computations have been carried out in double-precision arithmetic. As can be seen for each snapshot ensemble, the magnitude of the POD eigenvalues decays at a rapid rate for each subsequent POD vector (note logarithmic scale).

For the $\Delta\bar{\omega} = 0.0625$ snapshot ensemble, after approximately the first 30 POD vectors, the subsequent POD vectors have corresponding POD eigenvalues with magnitudes that tend to remain at a relatively constant level, 16 orders of magnitude less than the first POD shape eigenvalue magnitude, which is in fact the limit of the computer algorithm's double-precision arithmetic. These POD vectors turn out to be noise as a result of the finite precision and should not be used because they will have the tendency to corrupt the ROM. However, the first 30 POD vectors can be used. Thus, by using the POD eigenvalues as a measure, one can identify the appropriate POD vectors, which will best capture the unsteady dynamics of the system.

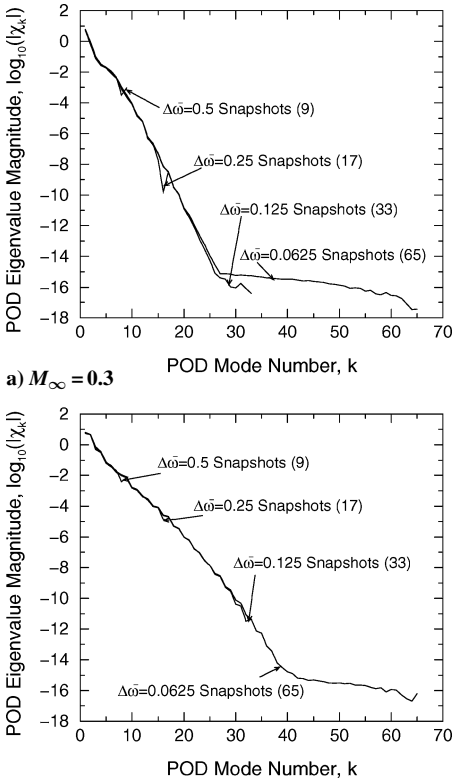


**Fig. 8 POD eigenvalues magnitude for different solution snapshot frequency resolutions: NACA 64A010 airfoil section, $\alpha_0 = 0$ (deg), 32 × 16 computational cells.**

To use the POD-derived full system eigenmodes to construct a ROM, one can approximate a full system eigenmode $\boldsymbol{r}_n$ using

$$\boldsymbol{r}_n = \boldsymbol{\Phi}\tilde{\boldsymbol{r}}_r, \qquad \boldsymbol{\Phi} = \begin{bmatrix} | & | & & | \\ \phi_1 & \phi_2 & \cdots & \phi_{N_P} \\ | & | & & | \end{bmatrix} \tag{24}$$

where $N_P$ is the number of POD vectors that one chooses to use from the total $N_S$ available POD vectors ($N_P \leq N_S$). How much smaller $N_P$ is compared to $N_S$ depends on how many DOF one wishes to retain, along with the level of accuracy desired. Also, if the POD eigenvalues indicate that some of the higher numbered POD shapes are noise, this will also limit the maximum value of $N_P$ as compared to $N_S$.

The eigenvalue problem defined by Eq. (6) can thus be written as

$$\boldsymbol{\Phi}^H(\boldsymbol{A}_0 - \tilde{\lambda}_n\boldsymbol{A}_1)\boldsymbol{\Phi}\tilde{\boldsymbol{r}}_n = \boldsymbol{0} \qquad \text{or} \qquad (\boldsymbol{\mathcal{A}}_0 - \tilde{\lambda}_n\boldsymbol{\mathcal{A}}_1)\tilde{\boldsymbol{r}}_n = \boldsymbol{0} \tag{25}$$

where $\boldsymbol{\mathcal{A}}_0$ and $\boldsymbol{\mathcal{A}}_1$ are $N_P \times N_P$ reduced versions of the original $\boldsymbol{A}_0$ and $\boldsymbol{A}_1$ matrices. These matrices can be rapidly computed with only $N_P$ steps of the flow solver (see Refs. 13 and 14 for more details). With $N_P$ small, the reduced-order system eigenvalues and eigenvectors of Eq. (25) are inexpensive to compute.

Figure 9 illustrates how the POD can be used in the case of the airfoil configuration to determine the dominant full system eigenmodes, which can in turn be used with the static/dynamic correction ROM. The first column of figures show the full system eigenvalues (open circles) and approximations of the full system eigenvalues (closed circles) when using POD vectors as described in the preceding paragraph. These cases correspond to using all of the available POD shapes when the snapshot ensembles consist of the $\Delta\bar{\omega} = 0.5$ (column 1), $\Delta\bar{\omega} = 0.25$ (column 2), and $\Delta\bar{\omega} = 0.125$ (column 3) intervals of snapshot frequency resolution.

The second column of figures show static/dynamic correction method ROM lift caused by pitch transfer function results when using only the least damped eigenmode for the ROM. Shown are results for the full system (open circles), the ROM when using the exact full system least damped eigenmode (filled circles), and the

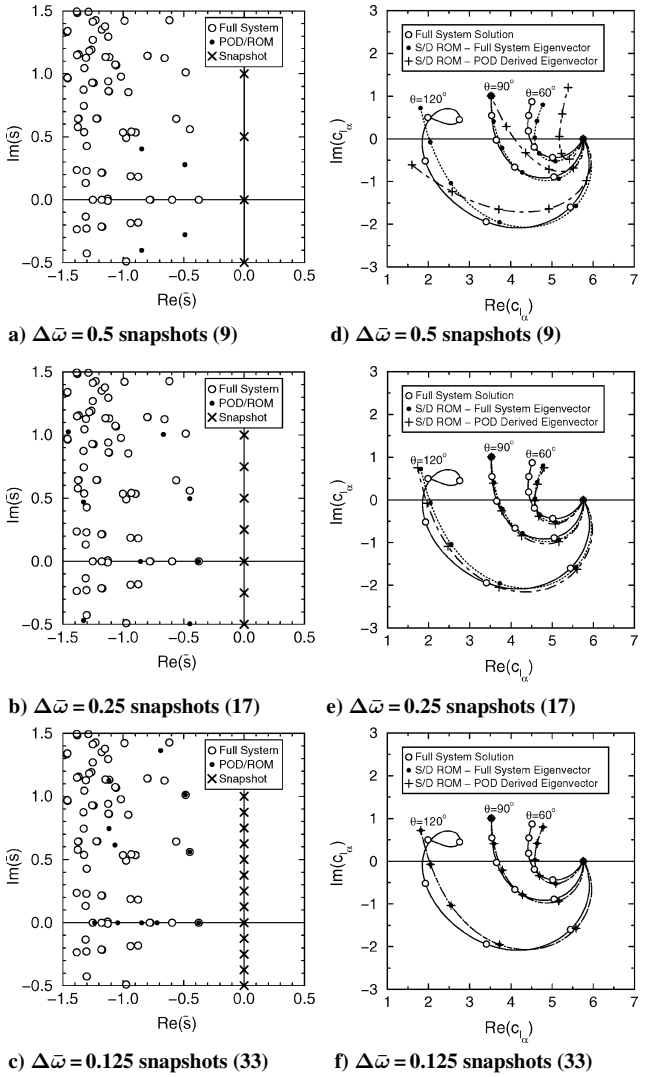


**Fig. 9 ROM characteristics for POD-derived eigenvectors: NACA 64A010 airfoil section, $M_\infty = 0.3$, $\alpha_0 = 0$ (deg), 32 × 16 computational cells.**

ROM when using the approximation of the least damped full system eigenmode via POD shape vectors (pluses).

As can be seen from the eigenspectrum plot, the $\Delta\bar{\omega} = 0.5$ snapshot ensemble does not provide a sufficient resolution to sufficiently reveal the least damped full system eigenmode. As a consequence, the transfer function results do not agree all that well with the results for the ROM when using the exact eigenmode. For the $\Delta\bar{\omega} = 0.25$ snapshot ensemble, the results are somewhat better. However, it is ultimately the $\Delta\bar{\omega} = 0.125$ ensemble, which has the necessary frequency resolution to enable the POD to be capable of revealing an accurate approximation of the exact full system least damped eigenvalue and corresponding eigenmode. When this occurs, the ROM based on the approximate eigenvalue can then be seen to agree very accurately with the exact eigenvalue ROM results.

The next issue to address is whether or not the static/dynamic correction ROM is an improvement over the POD/ROM method.[13,14] That is, is it worth the extra effort to derive the approximate system eigenmodes from the POD vectors to use with the static/dynamic correction ROM method, or is one better off simply using the POD/ROM approach.

Figures 10 and 11 show, for $M_\infty = 0.3$ and 0.9 respectively, a comparison of the full system and ROM forms of the lift caused by pitch transfer function when using various numbers of mode shapes for both the static/dynamic correction ROM and POD/ROM techniques. For both ROM strategies, and as a function of the number of modes shapes used, Figs. 10g and 11g show the $L_2$ error norm, for all four transfer functions (i.e., $\bar{c}_{l_{h/b}}$, $\bar{c}_{l_\alpha}$, $\bar{c}_{m_{h/b}}$, and $\bar{c}_{m_\alpha}$), along the

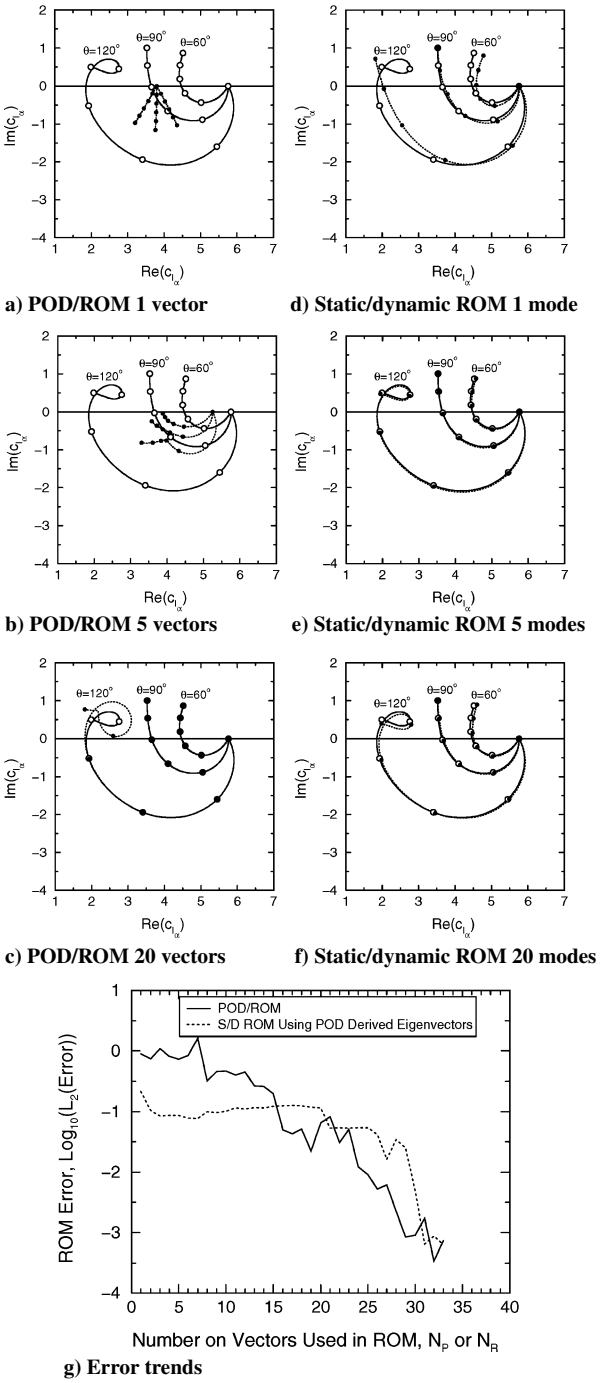


**Fig. 10 POD/ROM and static/dynamic correction ROM performance for $M_\infty = 0.3$: NACA 64A010 airfoil section, $\alpha_0 = 0$ (deg), 32 × 16 computational cells.**

specified paths in the complex frequency plane as shown in Fig. 2. For the $M_\infty = 0.3$ case, the static/dynamic correction ROM method can be seen to perform better than the POD/ROM technique up to approximately 15 modes. However for $M_\infty = 0.9$, one only achieves better performance when considering just a few modes in the ROM expansions.

Thus it is not a guarantee that the static/dynamic correction ROM method will always provide an advantage over the POD/ROM method. Whether it is advantageous has much to do with the Mach number under consideration along with the level of accuracy desired.

## Aeroelastic Wing Model

### AGARD 445.6 Wing Configuration

To demonstrate the static/dynamic ROM method for a very large CFD model, we next consider the AGARD 445.6 wing

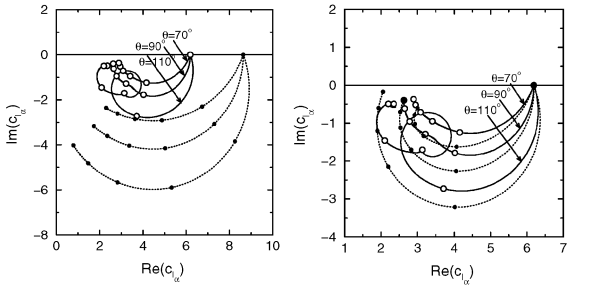


a) POD/ROM 1 vector




b) Static/dynamic ROM 1 mode

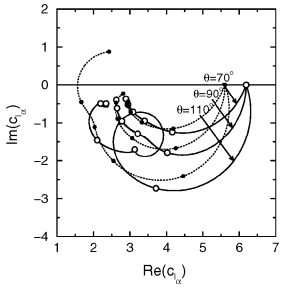


c) POD/ROM 5 vectors

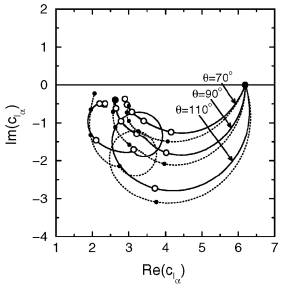


d) Static/dynamic ROM 5 modes

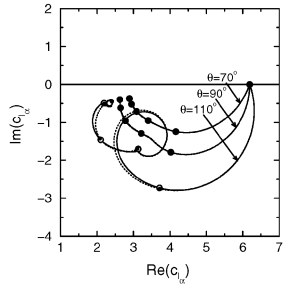


e) POD/ROM 20 vectors

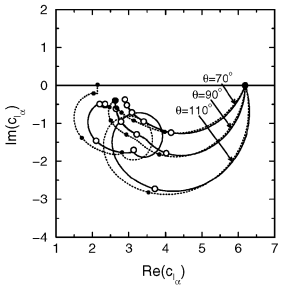


f) Static/dynamic ROM 20 modes

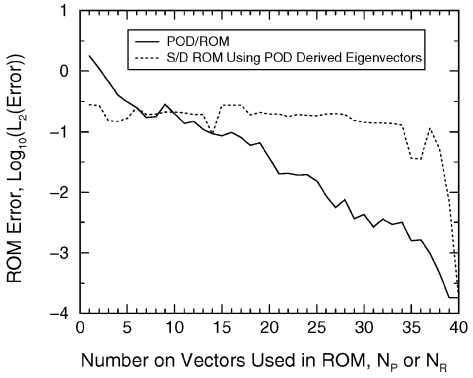


g) Error trends

**Fig. 11 POD/ROM and static/dynamic correction ROM performance for $M_\infty = 0.9$: NACA 64A010 airfoil section, $M_\infty = 0.9$, $\alpha_0 = 0$ (deg), 32 × 16 computational cells.**

configuration.[21,22] This is a 45-deg swept wing based on the NACA 65A004 airfoil section with an aspect ratio $A_R = 3.3$ and a taper ratio $\lambda_t = 2/3$. Figure 12 shows the computational mesh used for the CFD model of this configuration. The mesh is based on an O-O topology with 49 computational nodes about each airfoil section in the spanwise direction, 33 nodes normal to the wing surface, and 33 nodes along the semispan. The outer boundary of the mesh extends five semispans from the midchord of the wing-root section. The total number of fluid-dynamic DOF for this CFD model is 266,805.

### Wing Aeroelastic System of Governing Equations

We next couple the static/dynamic correction ROM method with the structural dynamic model for this configuration. We consider

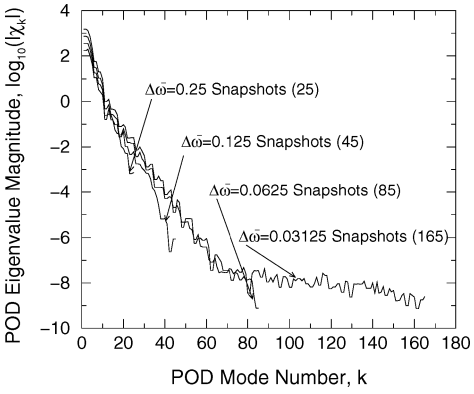


**Fig. 13 POD eigenvalues, 445.6 weak wing configuration, $M_\infty = 0.901$, $\alpha_0 = 0$ (deg).**

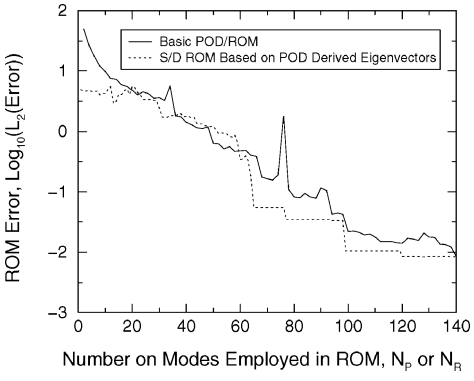


**Fig. 14 POD/ROM method and static/dynamic correction method error in modeling all 25 elements of generalized force coefficient transfer function matrix $\partial C_Q/\partial\xi(\bar{s})$ for frequencies corresponding to the snapshot frequencies, 445.6 weak wing configuration, $M_\infty = 0.901$, $\alpha_0 = 0$ (deg).**

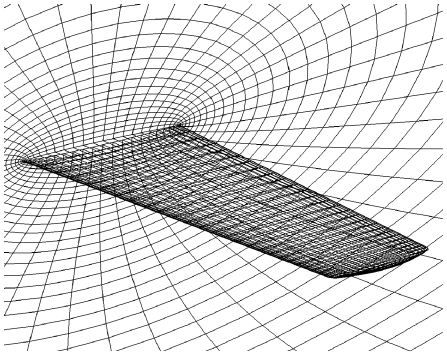

a) Wing surface and symmetry plane grids

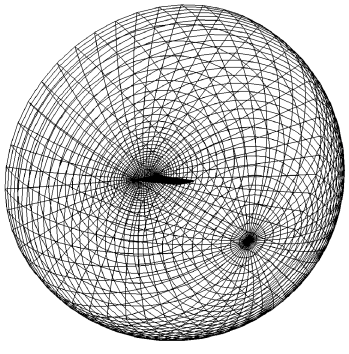

b) Outer boundary grid

**Fig. 12 AGARD 445.6 wing grid topology.**

the structural makeup (i.e., the mass and stiffness properties) of the AGARD 445.6 wing to correspond to what is referred as the "2.5 ft. weakened model 3" configuration (again see Refs. 21 and 22). The wing aeroelastic system of governing equations can be written as

$$\boldsymbol{\mathcal{M}}(\bar{s}^2\mu V^2\boldsymbol{I}+\boldsymbol{\Omega})\boldsymbol{\xi}=k_w V^2\boldsymbol{C}_{\mathcal{Q}}(\boldsymbol{\xi},\bar{s}) \tag{26}$$

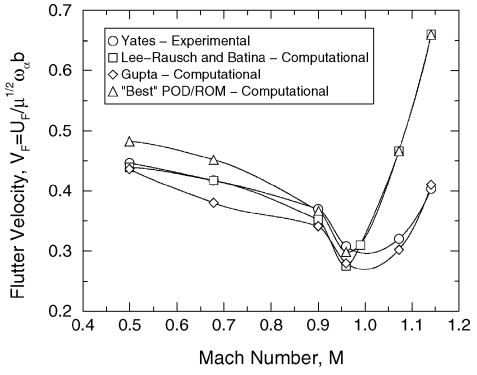


**Fig. 15 Mach-number flutter speed trend for the AGARD 445.6 wing weakened configuration, $\alpha_0 = 0$ (deg).**

where $k_w$ is a constant dependent on the wing shape and overall mass given by

$$k_w=\frac{6\bar{m}}{\pi A_R(1+\lambda_t)\left(1+\lambda_t+\lambda_t^2\right)} \tag{27}$$

$\boldsymbol{C}_{\mathcal{Q}}=\boldsymbol{\mathcal{Q}}/q_\infty c_r^2$ ($\boldsymbol{\mathcal{Q}}=\{\mathcal{Q}_1,\ldots,\mathcal{Q}_M\}^T$) is the vector of frequency dependent generalized aerodynamic force coefficients acting on the wing, and $\boldsymbol{\xi}=\{\xi_1,\ldots,\xi_M\}^T$ is the vector of $M$ structural modal coordinates. The generalized aerodynamic force coefficients can be written in matrix form as

$$\boldsymbol{C}_{\mathcal{Q}}=\underbrace{\left[\frac{\partial\boldsymbol{C}_{\mathcal{Q}}}{\partial\boldsymbol{\xi}}(\bar{s})\right]}_{M\times M}\boldsymbol{\xi}=\left[\frac{\partial C_{\mathcal{Q}_i}}{\partial\xi_j}\right]\boldsymbol{\xi} \tag{28}$$

where $\partial\boldsymbol{C}_Q/\partial\boldsymbol{\xi}(\bar{s})$ is the $M\times M$ matrix of aerodynamic transfer functions ($\partial C_{\mathcal{Q}_i}/\partial\xi_j$ being the coefficient of the $i$th generalized force caused by the $j$th structural modal coordinate) that we wish to approximate with the reduced-order modeling strategies.

### Transfer Function Approximation

The CFD method used for the AGARD 445.6 wing is a variant of the standard Lax–Wendroff scheme (see Refs. 23 and 24). The method happens to be second order in frequency, and thus the expansion for the static/dynamic correction ROM is somewhat more

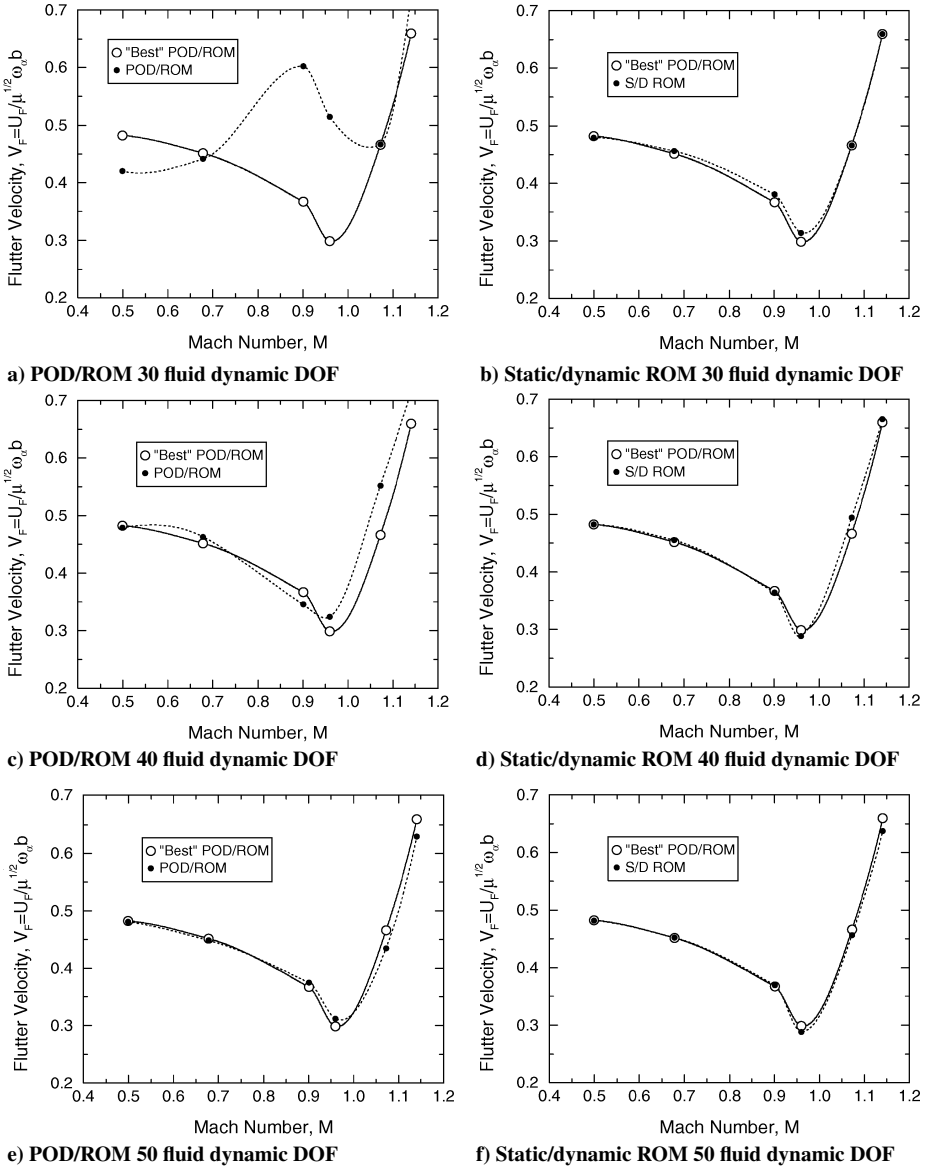


**a) POD/ROM 30 fluid dynamic DOF**

**b) Static/dynamic ROM 30 fluid dynamic DOF**

**c) POD/ROM 40 fluid dynamic DOF**

**d) Static/dynamic ROM 40 fluid dynamic DOF**

**e) POD/ROM 50 fluid dynamic DOF**

**f) Static/dynamic ROM 50 fluid dynamic DOF**

**Fig. 16 ROM Mach-number flutter speed trends for the AGARD 445.6 wing weakened configuration, $\alpha_0 = 0$ (deg).**

involved. The details are presented in the Appendix, where it is shown that the static/dynamic ROM for the generalized force transfer function matrix has the form

$$\boldsymbol{C}_{\mathcal{Q}} \approx \left(1-\frac{\bar{s}}{\bar{s}_d}\right)\left[\frac{\partial \boldsymbol{C}_{\mathcal{Q}}}{\partial \boldsymbol{\xi}}(0)\right]\boldsymbol{\xi} + \frac{\bar{s}}{\bar{s}_d}\left[\frac{\partial \boldsymbol{C}_{\mathcal{Q}}}{\partial \boldsymbol{\xi}}(\bar{s}_d)\right]\boldsymbol{\xi} + \left(\frac{\bar{s}^2}{\bar{s}_d}-\bar{s}\right)\underbrace{\boldsymbol{C}\boldsymbol{R}_{N_P}}_{M\times N_P}\underbrace{(\boldsymbol{\Lambda}_{N_P}-\bar{s}\boldsymbol{I})^{-1}}_{N_P\times N_P}\underbrace{\boldsymbol{L}_{N_P}\boldsymbol{B}}_{N_P\times M}\underbrace{\boldsymbol{\xi}}_{M\times 1} \tag{29}$$

If we introduce a vector of augmented variables $\boldsymbol{v}_{N_P}$ that satisfy the equation

$$(\boldsymbol{\Lambda}_{N_P}-\bar{s}\boldsymbol{I})\boldsymbol{v}_{N_P} + (1-\bar{s}/\bar{s}_d)\boldsymbol{L}_{N_P}\boldsymbol{B}(\bar{s}\boldsymbol{\xi}) = 0 \tag{30}$$

we can then write the ROM as

$$\boldsymbol{C}_{\mathcal{Q}} \approx \left(1-\frac{\bar{s}}{\bar{s}_d}\right)\left[\frac{\partial \boldsymbol{C}_{\mathcal{Q}}}{\partial \boldsymbol{\xi}}(0)\right]\boldsymbol{\xi} + \frac{\bar{s}}{\bar{s}_d}\left[\frac{\partial \boldsymbol{C}_{\mathcal{Q}}}{\partial \boldsymbol{\xi}}(\bar{s}_d)\right]\boldsymbol{\xi} + \underbrace{\boldsymbol{C}\boldsymbol{R}_{N_P}}_{M\times N_P}\underbrace{\boldsymbol{v}_{N_P}}_{N_P\times 1} \tag{31}$$

This leads to an aeroelastic system with $2M + N_P$ degrees of freedom

$$\left(\begin{bmatrix} \boldsymbol{E}_0 & \vdots & \boldsymbol{E}_1 & \vdots & \boldsymbol{C}\boldsymbol{R}_{N_P} \\ \cdots & & \cdots & & \cdots \\ & \vdots & \boldsymbol{I} & \vdots & \\ \cdots & & \cdots & & \cdots \\ & \vdots & \boldsymbol{L}_{N_P}\boldsymbol{B} & \vdots & \Lambda_{N_P} \end{bmatrix} - \bar{s}\begin{bmatrix} & \vdots & \boldsymbol{E}_2 & \vdots & \\ \cdots & & \cdots & & \cdots \\ & \vdots & \boldsymbol{I} & \vdots & \\ \cdots & & \cdots & & \cdots \\ & \vdots & \boldsymbol{L}_{N_P}\boldsymbol{B}/\bar{s}_d & \vdots & \boldsymbol{I} \end{bmatrix}\right)\begin{Bmatrix} \boldsymbol{\xi} \\ \bar{s}\boldsymbol{\xi} \\ \boldsymbol{v}_{N_P} \end{Bmatrix} = \begin{Bmatrix} 0 \\ 0 \\ 0 \end{Bmatrix} \tag{32}$$

where

$$\boldsymbol{E}_0 = \left[\frac{\partial \boldsymbol{C}_{\mathcal{Q}}}{\partial \boldsymbol{\xi}}(0)\right] - \frac{1}{k_w V^2}\boldsymbol{\mathcal{M}}\boldsymbol{\Omega}$$

$$\boldsymbol{E}_1 = \frac{1}{\bar{s}_d}\left(\left[\frac{\partial \boldsymbol{C}_{\mathcal{Q}}}{\partial \boldsymbol{\xi}}(\bar{s}_d)\right] - \left[\frac{\partial \boldsymbol{C}_{\mathcal{Q}}}{\partial \boldsymbol{\xi}}(0)\right]\right)$$

and

$$\boldsymbol{E}_2 = (\mu/k_w)\boldsymbol{\mathcal{M}}$$

**AGARD 445.6 Flutter Speed Prediction**

We begin by computing unsteady solution snapshots for a select number of Mach numbers, namely, $M_\infty = 0.499, 0.678, 0.901, 0.960, 1.072$, and $1.141$, which correspond to the experimental Mach numbers of Yates[21] and Yates et al.[22] The unsteady solution snapshots are based on wing motions corresponding to the first five structural mode shapes for the 2.5 ft. weakened model 3 structural configuration.[21,22] Snapshot reduced frequency intervals of $\Delta\bar{\omega} = 1/4, 1/8, 1/16$, and $1/32$ are considered for reduced frequencies ranging from 0 to 0.5. Figure 13 shows for the case of $M_\infty = 0.901$ the POD eigenvalue magnitude trends based on the snapshot ensembles for each of these four snapshot frequency resolutions. We have found the same basic trend holds for the other Mach numbers under consideration.

Next, based on the POD eigenvalue trends of Fig. 13, we have chosen to determine our approximate full system eigenvectors based on 70 of the 85 available POD shapes in the case of snapshots taken at incremental frequencies of $1/16 = 0.0625$. Because the CFD method is second order in frequency, this leads to a total of 140 snapshot/POD-derived approximate full system eigenvalues. Figure 14 shows error trends for the POD/ROM method and static/dynamic correction ROM method when using eigenvectors derived from the 70 POD shapes in modeling all 25 elements of generalized force coefficient transfer function matrix $\partial \boldsymbol{C}_Q/\partial \boldsymbol{\xi}(\bar{s})$. Here we consider frequencies corresponding to the snapshot frequencies. We are in effect measuring how well the ROM methods

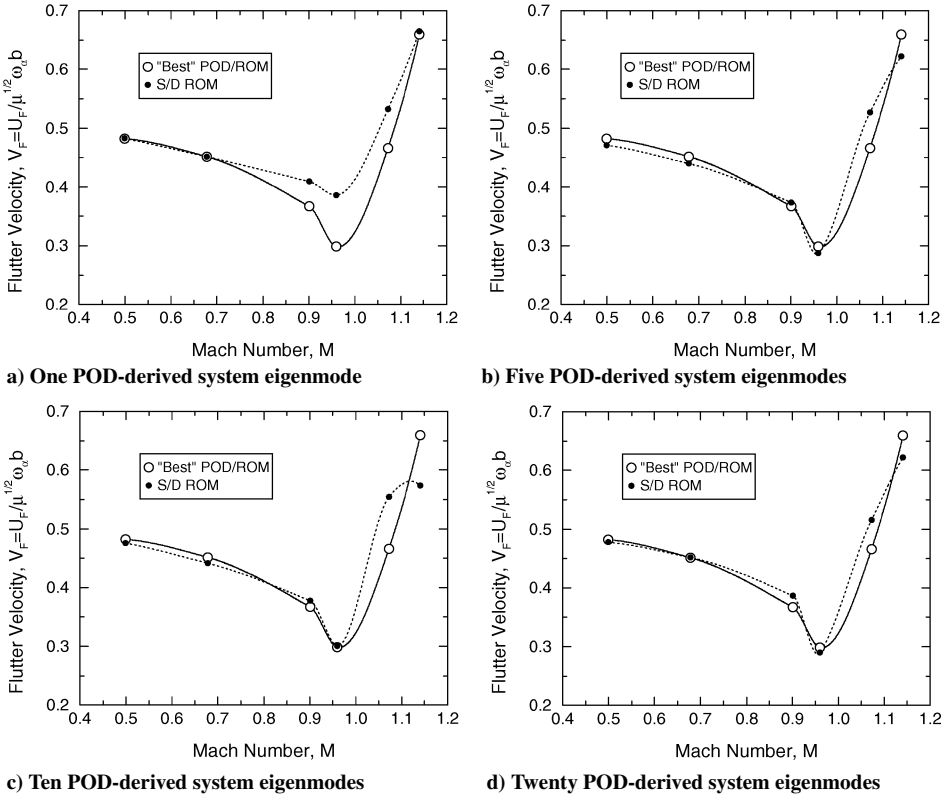


**a) One POD-derived system eigenmode** **b) Five POD-derived system eigenmodes**

**c) Ten POD-derived system eigenmodes** **d) Twenty POD-derived system eigenmodes**

**Fig. 17 Static/dynamic correction ROM Mach-number flutter speed trends for the AGARD 445.6 wing weakened configuration, $\alpha_0 = 0$ (deg).**

can reproduce the snapshots because they are all that we have in the way of an exact solution. As can be seen for this transonic wing configuration, the static/dynamic correction ROM method using eigenvectors derived from POD vectors is able to surpass the accuracy of the POD/ROM method for the first 20 modes shapes. Furthermore, it has comparable or even better accuracy for the higher modes. Similar trends can be shown for the other Mach numbers.

Figure 15 shows what we denote as our "best" POD/ROM computed flutter speed Mach-number trend (i.e., using 70 of 85 available POD shapes in the case of the $\Delta\bar{\omega} = 1/16$ frequency increment), along with the experimental data of Yates[21] and Yates et al.,[22] and the computational results of Lee-Rausch and Batina[25] and Gupta.[26] As can be seen, the transonic flutter speed dip is evident, and our results are all within the same tolerance to the results of the experimental and other computational methods. We will be addressing this particular configuration in more detail in a later publication. Here our primary objective is to demonstrate that our CFD solver, mesh, and structural model in conjunction with the ROM strategies are together capable of predicting the Mach-number flutter speed trend of a realistic three-dimensional transonic configuration.

To demonstrate how well the POD/ROM and static/dynamic correction ROM methods perform in modeling a global quantity such as flutter speed over a range of Mach numbers, Fig. 16 shows a comparison of the AGARD 445.6 wing POD/ROM and static/dynamic ROM computed flutter speed trend as compared to the best (70 POD shapes) POD/ROM method result when using various numbers of POD shapes (POD/ROM method) and POD derived system eigenmodes (static/dynamic correction ROM). As can be seen, the static/dynamic correction ROM produces favorable results in comparison to the POD/ROM method even when the number of fluid-dynamic modes is very small (30 approximate POD derived system eigenmodes).

Figure 17 illustrates computed AGARD 445.6 wing Mach-number flutter speed results when using the static/dynamic correction ROM with very few POD derived eigenmodes, in this instance, 1, 5, 10, and 20 POD derived approximate full system eigenmodes, which again have been determined from the 70 POD shape vectors. As can be seen, even these very small DOF models are able to yield good approximate results. By contrast, the POD/ROM results based on these same small numbers of DOF have such a large error that they do not even fall within the scales of these plots and therefore are not presented.

## Conclusions

A new static/dynamic correction approach for eigenvector-based reduced-order modeling (ROM) is presented. The method can be viewed as an alternative to single and multiple static correction ROM techniques, which are often used to improve the accuracy of a standard Ritz expansion eigenvector ROM. The method requires the computation of a single zero frequency, as is the case with the single static correction ROM, plus the computation of a single nonzero-frequency solution. The method is shown to have much better accuracy for a subsonic model case when compared to the standard Ritz expansion eigenvector ROM, a single static correction ROM, and a three static correction ROM. The method is also shown to have better accuracy for a transonic model case when compared to the standard Ritz expansion eigenvector ROM and a single static correction ROM, while having comparable accuracy with a three static correction ROM for the same problem. The main advantage of the static/dynamic correction ROM over the multiple static correction ROM is that static/dynamic correction ROM technique enables one to circumvent the necessity of having to determine the multiple static corrections, which require the formulation and solution of an alternate system of equations. The static/dynamic correction ROM only requires the computation of one additional nonzero frequency.

For large systems where determining eigenvalues and eigenvectors is prohibitive, POD vectors are shown to offer a convenient method for determining approximations of the least damped fluid-dynamic eigenmodes. These approximate eigenmodes can in turn be used with the static/dynamic correction approach to create a ROM, which in many cases has better accuracy than the straightforward POD/ROM method where POD shapes, as opposed to system eigenmodes, are used as shape vectors in a conventional Ritz expansion. The approximate eigenmode static/dynamic correction ROM is used to determine the flutter speed trend for a large system CFD model of a transonic aeroelastic wing configuration. Accurate results are demonstrated using just a few dozen POD approximated eigenmodes. Furthermore, up to the level of a few dozen modes, the static/dynamic correction ROM method is usually more accurate than the POD/ROM method.

## Appendix: Derivation of ROM Technique for a CFD Model Second Order in Frequency

Here we consider the case where the unsteady CFD model is second order in frequency. This leads to a fluid-dynamic system of equations having the form

$$\left(\boldsymbol{A}_0 + \bar{s}\boldsymbol{A}_1 + \bar{s}^2\boldsymbol{A}_2\right)\boldsymbol{q} = \left(\boldsymbol{B}_0 + \bar{s}\boldsymbol{B}_1 + \bar{s}^2\boldsymbol{B}_2\right)\boldsymbol{\xi} \tag{A1}$$

We begin by introducing state-space variables such that

$$\boldsymbol{q}' = \begin{Bmatrix} \boldsymbol{q} \\ \bar{s}\boldsymbol{q} \end{Bmatrix} \tag{A2}$$

The homogeneous case of Eq. (A1) can then be written as

$$\left(\boldsymbol{A}'_0 - \bar{s}\boldsymbol{A}'_1\right)\boldsymbol{q}' = \boldsymbol{0} \tag{A3}$$

where

$$\boldsymbol{A}'_0 = \begin{bmatrix} \boldsymbol{A}_0 & \boldsymbol{A}_1 \\ 0 & \boldsymbol{I} \end{bmatrix} \qquad \boldsymbol{A}'_1 = \begin{bmatrix} 0 & -\boldsymbol{A}_2 \\ \boldsymbol{I} & 0 \end{bmatrix} \tag{A4}$$

Let $\boldsymbol{R}'$ and $\boldsymbol{L}'$ be the matrices of right and left eigenvectors of the generalized eigenvalue problem defined by Eq. (A3), where

$$\boldsymbol{R}' = \begin{bmatrix} | & | & & | \\ \boldsymbol{r}'_1 & \boldsymbol{r}'_2 & \cdots & \boldsymbol{r}'_{2N} \\ | & | & & | \end{bmatrix} \qquad \boldsymbol{L}' = \begin{bmatrix} - & \boldsymbol{l}'_1 & - \\ - & \boldsymbol{l}'_2 & - \\ & \vdots & \\ - & \boldsymbol{l}'_{2N} & - \end{bmatrix} \tag{A5}$$

and normalized such that

$$\boldsymbol{L}'\boldsymbol{A}'_0\boldsymbol{R}' = \boldsymbol{\Lambda}' \qquad \boldsymbol{L}'\boldsymbol{A}'_1\boldsymbol{R}' = \boldsymbol{I} \tag{A6}$$

where $\boldsymbol{\Lambda}'$ is the matrix with the eigenvalues of Eq. (A3) situated along the diagonal. Additionally, let $\boldsymbol{T}$ be the $N \times 2N$ matrix that maps the state-space variables $\boldsymbol{q}'$ back to the unsteady small disturbance variables $\boldsymbol{q}$, namely,

$$\boldsymbol{T} = [\boldsymbol{I} \;\; 0] \tag{A7}$$

where $\boldsymbol{I}$ in this instance is the $N \times N$ identity matrix. Finally, let $\boldsymbol{C}$ be the $M \times N$ matrix that represents the operator for the discrete representation the integral of the loading and the structural modal coordinates that yields the $M$ generalized forces based on a given unsteady flow $\boldsymbol{q}$.

Using these definitions, it can be shown that the expression for the generalized forces $\boldsymbol{C}_Q$ via the basic Ritz eigenvector expansion approach is given by

$$\underbrace{\boldsymbol{C}_Q}_{M\times 1} = \underbrace{\boldsymbol{C}}_{M\times N}\underbrace{\boldsymbol{T}}_{N\times 2N}\underbrace{\boldsymbol{R}'}_{2N\times 2N}\underbrace{(\boldsymbol{\Lambda}' - \bar{s}\boldsymbol{I})^{-1}}_{2N\times 2N}\underbrace{\boldsymbol{L}'}_{2N\times 2N}\underbrace{\boldsymbol{T}^H}_{2N\times N} \times \underbrace{\left(\boldsymbol{B}_0 + \bar{s}\boldsymbol{B}_1 + \bar{s}^2\boldsymbol{B}_2\right)}_{N\times M}\underbrace{\boldsymbol{\xi}}_{M\times 1} \tag{A8}$$

The generalized forces $\boldsymbol{C}_Q$ using the static/dynamic correction ROM approach are given by

$$\underbrace{\boldsymbol{C}_Q}_{M\times 1} = \left(1 - \frac{\bar{s}}{\bar{s}_d}\right)\underbrace{\left[\frac{\partial \boldsymbol{C}_Q}{\partial \boldsymbol{\xi}}(0)\right]}_{M\times M}\underbrace{\boldsymbol{\xi}}_{M\times 1} + \frac{\bar{s}}{\bar{s}_d}\underbrace{\left[\frac{\partial \boldsymbol{C}_Q}{\partial \boldsymbol{\xi}}(\bar{s}_d)\right]}_{M\times M}\underbrace{\boldsymbol{\xi}}_{M\times 1} + \underbrace{\boldsymbol{C}}_{M\times N}\underbrace{\boldsymbol{T}}_{N\times 2N}\underbrace{\boldsymbol{R}'}_{2N\times 2N}\underbrace{\boldsymbol{v}}_{2N\times 1} \tag{A9}$$

where $\boldsymbol{v}$, sometimes referred to as the augmented aerodynamic state variables vector, is given by

$$\underbrace{\boldsymbol{v}}_{2N\times 1} = \bar{s}\left(\frac{\bar{s}}{\bar{s}_d} - 1\right)\underbrace{(\boldsymbol{\Lambda}' - \bar{s}\boldsymbol{I})^{-1}}_{2N\times 2N} \times \left[\underbrace{\left(\boldsymbol{\Lambda}' - \bar{s}_d\boldsymbol{I}\right)^{-1}}_{2N\times 2N}\underbrace{\boldsymbol{L}'}_{2N\times 2N}\underbrace{\boldsymbol{T}^H}_{2N\times N}\underbrace{\left(\boldsymbol{B}_0 + \bar{s}_d\boldsymbol{B}_1 + \bar{s}_d^2\boldsymbol{B}_2\right)}_{N\times M} + \bar{s}_d\underbrace{\boldsymbol{L}'}_{2N\times 2N}\underbrace{\boldsymbol{T}^H}_{2N\times N}\underbrace{\boldsymbol{B}_2}_{N\times M} - \underbrace{(\boldsymbol{\Lambda}')^{-1}}_{2N\times 2N}\underbrace{\boldsymbol{L}'}_{2N\times 2N}\underbrace{\boldsymbol{T}^H}_{2N\times N}\underbrace{\boldsymbol{B}_0}_{N\times M}\right]\underbrace{\boldsymbol{\xi}}_{M\times 1} \tag{A10}$$

If one chooses to use $N_R$ eigenmodes that have been derived via the snapshot/POD method using $N_P$ POD shapes that have in turn been derived from $N_S$ solution snapshots, the generalized forces $\boldsymbol{C}_{\mathcal{Q}}$ using the static/dynamic correction ROM approach are given by

$$\underbrace{\boldsymbol{C}_{\mathcal{Q}}}_{M\times 1} \approx \left(1 - \frac{\bar{s}}{\bar{s}_d}\right)\underbrace{\left[\frac{\partial \boldsymbol{C}_Q}{\partial \boldsymbol{\xi}}(0)\right]}_{M\times M}\underbrace{\boldsymbol{\xi}}_{M\times 1} + \frac{\bar{s}}{\bar{s}_d}\underbrace{\left[\frac{\partial \boldsymbol{C}_Q}{\partial \boldsymbol{\xi}}(\bar{s}_d)\right]}_{M\times M}\underbrace{\boldsymbol{\xi}}_{M\times 1} + \underbrace{\boldsymbol{C}}_{M\times N}\underbrace{\boldsymbol{\Phi}}_{N\times N_P}\underbrace{\tilde{\boldsymbol{T}}}_{N_P\times 2N_P}\underbrace{\tilde{\boldsymbol{R}}'_{N_R}}_{2N_P\times N_R}\underbrace{\tilde{\boldsymbol{v}}_{N_R}}_{N_R\times 1} \tag{A11a}$$

where

$$\underbrace{\tilde{\boldsymbol{v}}_{N_R}}_{N_R\times 1} = \bar{s}\left(\frac{\bar{s}}{\bar{s}_d} - 1\right)\underbrace{\left(\tilde{\boldsymbol{\Lambda}}'_{N_R} - \bar{s}\boldsymbol{I}\right)^{-1}}_{N_R\times N_R} \times \left[\underbrace{\left(\tilde{\boldsymbol{\Lambda}}'_{N_R} - \bar{s}_d\boldsymbol{I}\right)^{-1}}_{N_R\times N_R}\underbrace{\tilde{\boldsymbol{L}}'_{N_R}}_{N_R\times 2N_P}\underbrace{\tilde{\boldsymbol{T}}^H}_{2N_P\times N_P}\underbrace{\boldsymbol{\Phi}^H}_{N_P\times N}\underbrace{\left(\boldsymbol{B}_0 + \bar{s}_d\boldsymbol{B}_1 + \bar{s}_d^2\boldsymbol{B}_2\right)}_{N\times M} + \bar{s}_d\underbrace{\tilde{\boldsymbol{L}}'_{N_R}}_{N_R\times 2N_P}\underbrace{\tilde{\boldsymbol{T}}^H}_{2N_P\times N_P}\underbrace{\boldsymbol{\Phi}^H}_{N_P\times N}\underbrace{\boldsymbol{B}_2}_{N\times M} - \underbrace{\left(\tilde{\boldsymbol{\Lambda}}'_{N_R}\right)^{-1}}_{N_R\times N_R}\underbrace{\tilde{\boldsymbol{L}}'_{N_R}}_{N_R\times 2N_P}\underbrace{\tilde{\boldsymbol{T}}^H}_{2N_P\times N_P}\underbrace{\boldsymbol{\Phi}^H}_{N_P\times N}\underbrace{\boldsymbol{B}_0}_{N\times M}\right]\underbrace{\boldsymbol{\xi}}_{M\times 1} \tag{A11b}$$

and

$$\tilde{\boldsymbol{R}}' = \begin{bmatrix} | & | & & | \\ \tilde{\boldsymbol{r}}'_1 & \tilde{\boldsymbol{r}}'_2 & \cdots & \tilde{\boldsymbol{r}}'_{2N_P} \\ | & | & & | \end{bmatrix} \qquad \tilde{\boldsymbol{L}}' = \begin{bmatrix} - & \tilde{\boldsymbol{l}}'_1 & - \\ - & \tilde{\boldsymbol{l}}'_2 & - \\ & \vdots & \\ - & \tilde{\boldsymbol{l}}'_{2N_P} & - \end{bmatrix} \tag{A12}$$

such that the eigenvectors $\tilde{\boldsymbol{r}}'_n$ satisfy the generalized eigenvalue problem

$$\left(\tilde{\boldsymbol{A}}'_0 - \tilde{\lambda}_n\tilde{\boldsymbol{A}}'_1\right)\tilde{\boldsymbol{r}}'_n = 0 \tag{A13}$$

based on

$$\tilde{\boldsymbol{A}}'_0 = \begin{bmatrix} \boldsymbol{\mathcal{A}}_0 & \boldsymbol{\mathcal{A}}_1 \\ 0 & \boldsymbol{I} \end{bmatrix} \qquad \tilde{\boldsymbol{A}}'_1 = \begin{bmatrix} 0 & -\boldsymbol{\mathcal{A}}_2 \\ \boldsymbol{I} & 0 \end{bmatrix} \tag{A14}$$

and

$$\boldsymbol{\mathcal{A}}_0 = \boldsymbol{\Phi}^H\boldsymbol{A}_0\boldsymbol{\Phi} \qquad \boldsymbol{\mathcal{A}}_1 = \boldsymbol{\Phi}^H\boldsymbol{A}_1\boldsymbol{\Phi} \qquad \boldsymbol{\mathcal{A}}_2 = \boldsymbol{\Phi}^H\boldsymbol{A}_2\boldsymbol{\Phi} \tag{A15}$$

with the eigenvectors normalized such that

$$\tilde{\boldsymbol{L}}'\tilde{\boldsymbol{A}}'_0\tilde{\boldsymbol{R}}' = \tilde{\boldsymbol{\Lambda}}' \qquad \tilde{\boldsymbol{L}}'\tilde{\boldsymbol{A}}'_1\tilde{\boldsymbol{R}}' = \boldsymbol{I} \tag{A16}$$

## References


[1]Roger, K. L., "Airplane Math Modeling Methods for Active Control Design," AGARD-CP-228, Aug. 1977, pp. 4.1–4.11.

[2]Vepa, R., "On the Use of Padé Approximates to Represent Unsteady Aerodynamic Loads for Arbitrarily Small Motions of Wings," AIAA Paper 76-17, Jan. 1976.

[3]Edwards, J. W., "Applications of Laplace Transform Methods to Airfoil Motion and Stability Calculations," AIAA Paper 79-0772, April 1979.

[4]Karpel, M., "Design for Active Flutter Suppression and Gust Alleviation Using State-Space Aeroelastic Modeling," *Journal of Aircraft*, Vol. 19, No. 3, 1982, pp. 221–227.

[5]Dowell, E. H., Romanowski, M. C., and Hall, K. C., "Eigenmode Analysis in Unsteady Aerodynamics: Reduced Order Models," *Applied Mechanics Review*, Vol. 50, No. 6, 1997, pp. 371–386.

[6]Romanowski, M. C., and Dowell, E. H., "Using Eigenmodes to Form an Efficient Euler Based Unsteady Aerodynamics Analysis," *Aeroelasticity and Fluid*, edited by P. P. Friedman and C. I. Chang, WAM/IMECE Session Publication AD-44, G00 948, American Society of Mechanical Engineers, New York, Nov. 1994, pp. 147–160.

[7]Hall, K. C., "Eigenanalysis of Unsteady Flows About Airfoils, Cascades, and Wings," *AIAA Journal*, Vol. 32, No. 12, 1994, pp. 2426–2432.

[8]Hall, K. C., Florea, R., and Lanzkron, P. J., "A Reduced Order Model of Unsteady Flows in Turbomachinery," *Journal of Turbomachinery*, Vol. 117, No. 3, 1995, pp. 375–383.

[9]Florea, R., and Hall, K. C., "Eigenmode Analysis of Unsteady Flows about Airfoils," *Journal of Computational Physics*, Vol. 147, No. 2, Dec. 1998, pp. 568–593.

[10]Florea, R., Hall, K. C., and Dowell, E. H., "Eigenmode Analysis and Reduced Order Modeling of Unsteady Transonic Full Potential Flow Around Airfoils," *Journal of Aircraft*, Vol. 37, No. 3, 2000, pp. 454–462.

[11]Dowell, E. H., Hall, K. C., Thomas, J. P., and Florea, R., "Reduced Order Models in Unsteady Aerodynamics," *Engineering Mechanics*, Vol. 6, No. 4/5, 1999, pp. 229–252.

[12]Kim, T.,"Frequency-Domain Karhunen-Loeve Method and Its Application to Linear Dynamic Systems," *AIAA Journal*, Vol. 36, No. 11, 1998, pp. 2117–2123.

[13]Hall, K. C., Thomas, J. P., and Dowell, E. H., "Proper Orthogonal Decomposition Technique for Transonic Unsteady Aerodynamic Flows," *AIAA Journal*, Vol. 38, No. 10, 2000, pp. 1853–1862.

[14]Thomas, J. T., Dowell, E. H., and Hall, K. C., "Three-Dimensional Aeroelasticity Using Proper Orthogonal Decomposition Based Reduced Order Models," *Journal of Aircraft*, Vol. 40, No. 3, 2003, pp. 544–551.

[15]Godunov, S. K., "A Finite Difference Method of the Numerical Computation of Discontinuous Solutions of the Equations of Fluid Dynamics," *Matematicheskii Sbornik*, Vol. 47, 1959, pp. 357–393.

[16]Roe, P. L., "Approximate Riemann Solvers, Parameter Vectors, and Difference Schemes," *Journal of Computational Physics*, Vol. 43, No. 2, 1981, pp. 357–372.

[17]van Leer, B., "Towards the Ultimate Conservative Difference Scheme, II. Monotonicity and Conservation Combined in a Second-Order Scheme," *Journal of Computational Physics*, Vol. 14, No. 4, 1974, pp. 361–376.

[18]Anderson, E., Bai, Z., Bischof, C., Blackford, S., Demmel, J., Dongarra, J., Du Croz, J., Greenbaum, A., Hammarling, S., McKenney, A., and Sorensen, D., *LAPACK Users' Guide*, 3rd ed., Society of Industrial and Applied Mathematics, Philadelphia, PA, 1999.

[19]Lehoucq, R. B., Sorensen, D. C., and Yang, C., *ARPACK Users' Guide: Solution of Large-Scale Eigenvalue Problems with Implicitly Restarted Arnoldi Methods, Software, Environments, and Tools 6*, Society of Industrial and Applied Mathematics, Philadelphia, PA, 2000.

[20]Holmes, P., Lumley, J. L., and Berkooz, G., *Turbulence, Coherent Structures, Dynamical Systems and Symmetry*, Cambridge Univ. Press, Cambridge, England, U.K., 1996.

[21]Yates, E. C., Jr., "AGARD Standard Aeroelastic Configurations for Dynamic Response I—Wing 445.6," AGARD-R-765, 1985, pp. 1–73.

[22]Yates, E. C., Jr., Land, N. S., and Foughner, J. T., Jr., "Measured and Calculated Subsonic and Transonic Flutter Characteristics of a 45 Deg Sweptback Wing Planform in Air and in Freon-12 in the Langley Transonic Dynamics Tunnel," NASA TN D-1616, March 1963.

[23]Ni, R., "A Multiple Grid Scheme for Solving the Euler Equations," *AIAA Journal*, Vol. 20, No. 11, 1982, pp. 1565–1571.

[24]Saxor, A. P., "A Numerical Analysis of 3-D Inviscid Stator/Rotor Interactions Using Non-Reflecting Boundary Conditions," MIT, Gas Turbine Lab., Rept. 209, Cambridge, MA, March 1992.

[25]Lee-Rausch, E. M., and Batina, J. T., "Wing Flutter Boundary Prediction Using Unsteady Euler Aerodynamic Method," *Journal of Aircraft*, Vol. 32, No. 2, 1995, pp. 416–422.

[26]Gupta, K. K., "Development of a Finite Element Aeroelastic Analysis Capability," *Journal of Aircraft*, Vol. 33, No. 5, 1996, pp. 995–1002.